JGR Atmospheres

RESEARCH ARTICLE
10.1029/2022JD037312

North Atlantic Tropical Cyclone Size and Storm Surge Reconstructions From 1950-Present

Avantika Gori[1], Ning Lin[1], Benjamin Schenkel[2,3], and Daniel Chavas[4]

[1]Department of Civil and Environmental Engineering, Princeton University, Princeton, NJ, USA, [2]School of Meteorology, The Cooperative Institute for Severe and High-Impact Weather Research and Operations, University of Oklahoma, Norman, OK, USA, [3]NOAA/OAR National Severe Storms Laboratory, Norman, OK, USA, [4]Department of Earth, Atmospheric, and Planetary Sciences, Purdue University, West Lafayette, IN, USA

Abstract Tropical cyclones (TCs) are one of the greatest threats to coastal communities along the US Atlantic and Gulf coasts due to their extreme wind, rainfall and storm surge. Analyzing historical TC climatology and modeling TC hazards can provide valuable insight to planners and decision makers. However, detailed TC size information is typically only available from 1988 onward, preventing accurate wind, rainfall, and storm surge modeling for TCs occurring earlier in the historical record. To overcome temporally limited TC size data, we develop a database of size estimates that are based on reanalysis data and a physics-based model. Specifically, we utilize ERA5 reanalysis data to estimate the TC outer size, and a physics-based TC wind model to estimate the radius of maximum wind. We evaluate our TC size estimates using two high-resolution wind data sets as well as Best Track information for a wide variety of TCs. Using the estimated size information plus the TC track and intensity, we reconstruct historical storm tides from 1950 to 2020 using a basin-scale hydrodynamic model and show that our reconstructions agree well with observed peak storm tide and storm surge. Finally, we demonstrate that incorporating an expanded set of historical modeled storm tides beginning in 1950 can enhance our understanding of US coastal hazard. Our newly developed database of TC sizes and associated storm tides/surges can aid in understanding North Atlantic TC climatology and modeling TC wind, storm surge, and rainfall hazard along the US Atlantic and Gulf coasts.

Plain Language Summary Tropical cyclones (TCs) threaten coastlines with their extreme wind, rainfall, and storm surges. To model historical TCs and their hazards, accurate storm size information is needed. However, size information is only available from 1988-onward, preventing accurate modeling of earlier TCs. Here, we utilize reanalysis data and a physics-based TC wind model to reconstruct TC sizes for North Atlantic storms from 1950-present. We then utilize a hydrodynamic ocean model to reconstruct historical TC storm surges across the US Atlantic and Gulf coasts from 1950-present. We demonstrate that our expanded historical storm surge reconstructions can enhance understanding of coastal risk. Furthermore, our reconstructed TC sizes can facilitate modeling of historical TC wind and rainfall hazard for pre-1988 storms.

Key Points:

- We leverage ERA5 reanalysis data combined with a physics-based wind model to estimate tropical cyclone (TC) storm size
- We develop a data set of North Atlantic TC storm sizes (i.e., radius to maximum wind and outer size) from 1950 to 2020
- Using reconstructed TC sizes and a hydrodynamic model, we develop a data set of historical storm tides from 1950 to 2020

Supporting Information:

Supporting Information may be found in the online version of this article.

Correspondence to:

A. Gori,
agori@princeton.edu

Citation:

Gori, A., Lin, N., Schenkel, B., & Chavas, D. (2023). North Atlantic tropical cyclone size and storm surge reconstructions from 1950-present. *Journal of Geophysical Research: Atmospheres*, *128*, e2022JD037312. https://doi.org/10.1029/2022JD037312

Received 15 JUN 2022
Accepted 13 FEB 2023

1. Introduction

Tropical cyclones (TCs) are one of the largest threats to coastal communities worldwide (Dullaart et al., 2021), and are the costliest natural hazard impacting the United States (Smith & Katz, 2013). Landfalling TCs can bring extreme wind, storm surge, and rainfall to coastal regions, resulting in widespread damage and loss of life. For example, the Galveston hurricane of 1900 caused at least 6,000 fatalities, and remains the deadliest US hurricane to date (Cline, 1900). More recently, Hurricanes Katrina (2005), Sandy (2012), and Harvey (2017) caused extreme flooding due to their rainfall and storm surge with total damages ranging from $80 to $150 billion (2022 USD) for each of the storms (Blake & Zelinsky, 2017; Blake et al., 2013; Knabb et al., 2005). Given the magnitude and frequency of TC-induced catastrophes, it is vital to understand and characterize the wind, rain and surge hazards from historical hurricanes. Developing spatially and temporally continuous records of TC storm characteristics and associated hazards can aid in risk assessment, emergency planning, and mitigation efforts.

TC wind, rainfall and surge severity in coastal regions depends on storm characteristics including intensity (maximum sustained wind speed—V_{max} and minimum central pressure—P_{min}), inner size (i.e., radius to maximum wind—R_{max}), translation speed, and approach angle to the coast (Irish et al., 2008; Ramos-Valle et al., 2020; Thomas et al., 2019). Peak storm surges also vary based on geographic characteristics, such as coastline shape

and near-shore bathymetry (Woodruff et al., 2013), while rainfall rates are sensitive to topography and land cover characteristics (Zhang et al., 2018). Aside from features of the synoptic-scale environment (such as vertical wind shear), V_{max} and R_{max} are often the two most important storm characteristics controlling the TC wind field (Chavas et al., 2015), peak rainfall rate (Liu et al., 2019), and peak storm surge (Bass et al., 2017).

Databases of North Atlantic TC tracks and intensities, such as the International Best Track Archive for Climate Stewardship (IBTrACS; Knapp et al., 2010), date back to the 1800's. However, detailed TC size estimates are typically only available from 1988 onward (Demuth et al., 2006) and wind radii are only best tracked (i.e., reviewed post season) from 2004 onward, although R_{max} is only reviewed from 2021 onwards. There are also numerous databases containing information about observed TC storm surge and rainfall. For example, several databases of observed storm tides from tidal gauges (https://tidesandcurrents.noaa.gov) and high-water marks (https://stn.wim.usgs.gov/FEV) are available, and these observations can provide valuable hazard information. However, their spatial and temporal coverage is limited: along the US coastline there are only 100 tidal gauges with more than 30 years of data. The relatively sparse distribution of tidal gauges may not capture peak water levels induced by TCs (Haigh et al., 2014; Pugh, 1987), and these gauges may fail during high intensity events (Beven et al., 2008; Fritz et al., 2007). Other storm surge databases drawing from observations, technical reports, journal articles, and newspapers (Needham & Keim, 2012; Needham et al., 2015) have estimated the location and magnitude of peak storm surges for many historical TCs, although they do not provide spatially continuous storm surge estimates for each event. As with storm surge observations, peak wind speed and rainfall observations are available at gauge locations (Menne et al., 2012) dating back to the late 1800's. However, spatially continuous, sub-daily wind field or rainfall observations, such as data derived from satellite and radar, is only available starting in the late 1990's (Chavas & Vigh, 2014; Huffman et al., 2021; Y. Lin & Mitchell, 2005; Powell et al., 1998). Moreover, since satellite data is often only available at irregular sampling intervals, snapshots of wind and rainfall estimates from satellite products may not be temporally continuous. Given the dearth of observations, we can instead use physics-based wind models, rainfall models, and high-resolution hydrodynamic models to reconstruct spatially and temporally continuous estimates of historical TC hazards and structure. Currently, model-based data sets of historical TC storm tides and winds only date back to 1988 (Done et al., 2020; Marsooli & Lin, 2018; Muis et al., 2019) due to temporally limited TC size data. Expanding these data sets to incorporate hazard estimates from earlier TCs would greatly enhance our understanding of historical TC risk.

To overcome temporally limited TC size data, reanalysis data sets, which are hindcasts using a static version of operational numerical weather prediction models (Thorne & Vose, 2010), and physics-based TC models may be used together to estimate wind field structure. Typical global reanalysis products, with horizontal grid resolution ranging from 0.25° to 0.7°, are often unable to resolve the TC inner core (Hodges et al., 2017; Schenkel & Hart, 2012). However, these data sets may be able to accurately represent features of the outer TC wind field (Bian et al., 2021; Schenkel et al., 2017), where winds are weak, convection is sparse, and the troposphere is approximately in radiative-subsidence balance (Chavas et al., 2015). The size of the outer TC wind field is often defined as the radius of the outermost closed isobar (Merrill, 1984), radius of a specified azimuthal-mean weak 10-m wind speed (e.g., radius of 2–12 m/s azimuthal winds; Chavas & Vigh, 2014; Chavas et al., 2016; Schenkel et al., 2018, 2017), or radius to tropical storm force winds (Chavas & Knaff, 2022). Previous studies have found that reanalysis data sets can reasonably represent TC outer size metrics, such as radii of azimuthal-mean 6–8 m/s azimuthal winds (Bian et al., 2021; Schenkel et al., 2017). Using reanalysis-based estimates of TC outer size and V_{max} based on Best Track data, parametric TC wind models may be used to characterize the full TC wind field. Specifically, the physics-based complete TC wind model of Chavas et al. (2015; hereafter CLE15) can realistically reproduce the entire TC wind field structure including hard to measure quantities like R_{max} based on outer size and V_{max} (Chavas et al., 2015; N. Lin & Chavas, 2012). Recently, Chavas and Knaff (2022) demonstrated how the CLE15 theory is quite similar to observations. They created a simple physics-based empirical model to estimate R_{max} from the radius of 17.5 m/s (34 knots) wind that compares well against R_{max} observations from historical North Atlantic TCs.

In this study, we leverage reanalysis-based estimates of TC outer size and the physics-based CLE15 wind model to reconstruct North Atlantic historical TC wind fields from 1950 to 2020 and model their associated storm tides using a high-resolution hydrodynamic model. We develop the first spatiotemporally continuous databases of R_{max} estimates for North Atlantic TCs from 1950 to 2020 and associated peak storm tides/surges for the US Atlantic and Gulf coastline. Our database can supplement size estimates from IBTrACS or the Extended Best Track Database (EBTRK; Demuth et al., 2006) for storms occurring earlier than 1988 and can supplement previous

storm tide databases (Marsooli & Lin, 2018; Muis et al., 2019) by similarly providing storm tide reconstructions for TCs occurring from 1950 onward. To evaluate our outer size and R_{max} estimates, we compare against two high-resolution TC wind field databases as well as against IBTrACS data. We evaluate the accuracy of our size estimates for the full TC life cycle of storms in both the low (equatorward of 30°N) and middle (poleward of 30°N) latitudes, and we investigate the uncertainty in the size estimates for storms undergoing extratropical transition (ET). Storm tide and surge reconstructions are compared against observed water levels from tidal gauges along the US coastline. Finally, we demonstrate how our storm tide reconstructions impact storm surge hazard assessment at various US cities.

2. Methods

2.1. TC Data Sets

North Atlantic TC track, intensity, and pressure information from 1950 onward are obtained from the IBTrACS data version 4, revision 0 (Knapp et al., 2010), which includes reanalyzed HURDAT2 storms (Delgado et al., 2018) until 1965. To focus on TCs that can cause non-negligible storm surges, we select storms with maximum wind speed greater than 17 m/s that approach within 200 km of the US coastline, resulting in 467 storms.

To estimate the outer TC wind field, we utilize the 0.25° latitude × 0.25° longitude 3-hr European Center for Medium-range Weather Forecasts (ECMWF) ERA5 reanalysis data set and back-extension (Hersbach et al., 2020). We choose the ERA5 reanalysis due to its relatively fine horizontal grid spacing compared to other reanalysis data sets, its long temporal coverage (1950–2020), and because previous work (Bian et al., 2021) demonstrated improved outer size representation of ERA5 compared to previous ERA versions. We determine the position of each TC within the reanalysis grid by using the IBTrACS position as a first guess. Then, using the sea-level pressure reanalysis fields we calculate the centroid of pressure deficit and iteratively adjust the estimated TC center position based on the method of Nguyen et al. (2014). Once given a center, we calculate the azimuthal-mean wind field and calculate the radius of a given weak wind speed to define storm size (details below).

We utilize the main ERA5 data set for 1959–2020 and the preliminary back-extension for 1950–1958. Due to the lack of satellite data pre-1980, TC track, intensity, and reanalysis-based outer size estimates from 1950 to 1979 have higher uncertainty compared to storms occurring from 1980 onward. Consequently, storm tide estimates for pre-1980 TCs also have higher uncertainty compared to post-1980 storms. Despite larger uncertainties associated with size estimates from the pre-satellite time period, a comparison of the ERA5 size distributions pre- and post-1979 demonstrates that both groups of storms have similar outer size climatologies (Figure S1 in Supporting Information S1) and similar R_{max} climatology (Figure S2 in Supporting Information S1). Due to the ERA5 back-extension data assimilation approach, some TCs are represented with unrealistically intense P_{min} values in the reanalysis data (ECMWF, 2021). We do not utilize reanalysis-based P_{min} or V_{max} estimates in our study, and only utilize features of the outer TC wind field from the reanalysis data. Still, the overly intense back-extension P_{min} values could have a small impact on the reanalysis representation of the outer TC wind field (see Figure S3 in Supporting Information S1 and associated discussion in caption). Since R_{max} values are not highly sensitive to small differences in outer size stemming from differences between the ERA5 back-extension and primary ERA5 data sets (Figure S4 in Supporting Information S1), here we use the back-extension to estimates TC sizes from 1950 to 1958. However, size estimates (especially outer sizes) for pre-1959 TCs likely have higher uncertainty compared to post-1959 TCs, and users of our data set should take this into consideration in their analyses. As subsequent ERA5 versions are released that ultimately extend back to 1940, our estimated size and storm surge data set will be expanded and updated.

To validate reanalysis TC size estimates, we compare against IBTrACS and two detailed TC wind field databases: the QuikSCAT Tropical Cyclone Radial Structure database (QSCAT-R; Chavas & Vigh, 2014) and the HWind database (Powell et al., 1998). Both QSCAT-R and HWind have been widely used to investigate features of the inner (Chavas & Lin, 2016) and outer (Bian et al., 2021; Chavas et al., 2016; Schenkel et al., 2017) wind fields of historical TCs. QSCAT-R contains snapshots of azimuthal-mean 10-m azimuthal winds from 167 North Atlantic TCs between 2000 and 2009, and has a horizontal grid spacing of approximately 12.5 km. The HWind data used here comes from 120 North Atlantic TCs spanning 2004–2013 with approximate horizontal grid spacing of 6 km. QSCAT-R wind fields, which are based on NASA's QuikSCAT satellite (Chavas & Vigh, 2014), are available at irregular time points during each TC, while the HWind data is provided at 6-hr intervals. QuikSCAT

tends to underestimate wind speeds in high wind regimes (Stiles et al., 2014) and is therefore more suitable for investigating features of the outer TC wind field. We utilize the QSCAT-R data set to validate the outer TC size estimates and use the higher resolution HWind data set and IBTrACS data from 2004 to 2020 to validate the R_{max} estimates. Importantly, R_{max} estimates from IBTrACS are not reanalyzed post-storm and are based on near real-time information from aircraft reconnaissance (when available) or remotely sensed data. Therefore, the IBTrACS R_{max} values may have significant uncertainty or errors, especially in the absence of in situ data. We utilize estimates of the IBTrACS R_{max} uncertainty that were developed by the National Hurricane Center (NHC) based on the 2021 North Atlantic and Northeast Pacific TC season. The uncertainty estimates are based on mean absolute errors (MAEs) for the Best Track R_{max} values and are binned according to TC intensity (Table S1 in Supporting Information S1). The MAEs used here assume each storm is observed by both satellite and aircraft reconnaissance, which is typical of landfalling TCs. Therefore, they represent conservative estimates of uncertainty as points far from land or without aircraft/satellite observations likely have much higher uncertainty. Moreover, as these estimates are derived from 2021 data, older storms in the IBTrACS data set likely also have higher uncertainty. Nevertheless, the Best Track R_{max} errors described here provide a benchmark we can use to evaluate our model-based R_{max} estimates.

2.2. TC Outer Size Estimation

Following Schenkel et al. (2017), we incorporate six outer size metrics defined as the radii at which the 10-m azimuthal-mean azimuthal wind speed equals 2, 4, 6, 8, 10, and 12 m/s (denoted r_2–r_{12}). We consider a range of size metrics since not all wind radii may be defined at every point in time in the reanalysis data. To estimate each size metric at each point in time, we follow Chavas and Vigh (2014) by first interpolating the reanalysis zonal and meridional winds to a TC-relative polar coordinate, excluding all grid points over land. A uniform environmental wind is then removed from the TC-relative zonal and meridional winds, which is estimated as 55% of the translation speed and rotated 20° counterclockwise according to N. Lin and Chavas (2012). An asymmetry parameter (χ) is also calculated at each radius according to Chavas and Vigh (2014). The χ parameter varies from 0 (perfect data symmetry about the TC center) to 1 (complete asymmetry about the TC center) and quantifies the degree of data coverage asymmetry at each radial distance. Radial bins with $\chi > 0.5$ are excluded from the outer size estimation (Chavas & Vigh, 2014). The azimuthal-mean azimuthal wind is then calculated, and followed by the extraction of outer size metrics (i.e., r_2, r_4, r_6, r_8, r_{10}, r_{12}).

The reanalysis outer size estimates may be biased compared to the observations, especially for r_{10} and r_{12} metrics (Bian et al., 2021; Schenkel et al., 2017). Therefore, we bias correct each outer size metric based on the comparison with the QSCAT-R outer sizes for the period between 2000 and 2009. We find that the average outer size bias is generally constant across the range of outer sizes for most size metrics (Figure S5 in Supporting Information S1), implying that the outer size estimates can be corrected by simply adding a single correction value to each estimate for a given metric. For each size metric (i.e., r_2–r_{12}), the median difference between the QSCAT-R values and the ERA5 estimates (shown as the horizontal red lines in Figure 2a) are calculated and added to each ERA5 size estimate, similar to Bian et al. (2021). Bias correction is applied to outer size estimates for all TCs from 1950 onward.

2.3. Physics-Based TC Wind Model and R_{max} Estimation

Several parametric TC wind models have been developed to represent the radial profile of wind speed, and most models require free-fitting parameters as well as estimates of V_{max} and R_{max} (Emanuel & Rotunno, 2011; Holland, 1980; Willoughby et al., 2006). In contrast, the more recently developed CLE15 complete wind profile is a fully physics-based model that describes the full TC wind field by merging solutions for the inner convective region and the outer descending region. Wang et al. (2022a) found that the CLE15 model better reproduces observed TC wind fields compared to the popularly used Holland model (Holland, 1980). As explained in Chavas and Lin (2016), the CLE15 wind profile can be constructed using V_{max} and a single additional outer wind radius with no arbitrary empirical parameters. Chavas and Lin (2016) also demonstrated that CLE15 profiles based on V_{max} and outer size were able to reproduce the observed wind field variability of historical North Atlantic TCs. Therefore, we use the CLE15 model to construct the full wind profile and extract an estimate for R_{max} using the reanalysis-based outer size estimates and V_{max} from IBTrACS. More details about the CLE15 model formulation are documented in Chavas et al. (2015).

2.4. Time Series of TC Size Estimates

A time series of R_{max} estimates are developed for each TC from 1950 to 2020 to match the IBTrACS time steps. For each 3-hr increment, the TC outer size metrics (r_2–r_{12}) are estimated from the ERA5 reanalysis data, and bias corrected as explained above. Next, the maximum azimuthal-mean azimuthal wind (V^*_{max}) is calculated based on the IBTrACS V_{max} ($V_{max,BT}$) as follows:

$$V^*_{max} = 0.75(V_{max,BT} - 0.55V_{trans}) \quad (1)$$

where V_{trans} is the TC translation speed. We remove the background wind, estimated as 55% of the storm translation speed (N. Lin & Chavas, 2012), from $V_{max,BT}$ and then apply an additional 0.75 reduction factor similar to the reduction factor of 0.8 used in Chavas et al. (2016). This additional reduction factor takes into account that $V_{max,BT}$ represents the maximum wind speed occurring at any point in the TC, while the CLE15 model takes the maximum azimuthal-mean azimuthal wind speed as input. The 0.75 reduction factor was developed by comparing the IBTrACS V_{max} estimates for all TCs from 2004 to 2013 with at least tropical storm intensity (>17 m/s) against the HWind maximum azimuthal-mean azimuthal wind speeds (Figure S6 in Supporting Information S1). Since the HWind data may be biased low compared to the Best Track V_{max} for very intense storms (Klotz & Nolan, 2019; Uhlhorn & Nolan, 2012), we conduct a sensitivity test by only using HWind points whose point-maximum wind speed is within 5% of the Best Track V_{max} (minus background wind) to calculate the reduction factor. We find that the re-calculated reduction factor is 0.76 (compared to 0.75 using all HWind points), indicating that it is not sensitive to small biases in the HWind data.

Using each outer size estimate and V^*_{max}, we construct a radial profile of azimuthal-mean 10-m TC azimuthal winds using the CLE15 wind model and estimate R_{max}. If more than three outer size metrics are undefined for a particular time step, R_{max} is set as undefined. Since the CLE15 model may produce different R_{max} estimates using different outer size metrics, we create a weighted average R_{max} based on all defined outer size metrics with weights proportional to the inverse of the root mean square error between the reanalysis outer size estimates and the QSCAT-R outer size estimates (Table S2 in Supporting Information S1). Alternately, if the performance against observations (see Figure S5 in Supporting Information S1) is similar for all outer size metrics, equal weights could be used to estimate R_{max}. Once the TC makes landfall, we do not utilize the reanalysis data to estimate outer size since our methodology sets reanalysis 10-m wind speeds over land are as undefined. Instead, we assume constant outer size after landfall equal to the last outer size estimate before landfall. Although TC size can change significantly after landfall (Chen & Chavas, 2020; Hlywiak & Nolan, 2021) and the TC wind field can become increasingly asymmetric as the storm weakens, our primary goal is to reconstruct TC storm surges, which would be minimally impacted by size and asymmetric changes occurring after landfall. The R_{max} at each point after landfall is estimated using V^*_{max} and constant outer size. Finally, we apply linear interpolation to fill in time steps where R_{max} is undefined due to insufficient outer size data, leading to a continuous time history of R_{max} values for each TC.

2.5. Defining Extratropical Transition (ET) Storms

Our study defines ET using the cyclone phase space (Evans & Hart, 2008; Hart, 2003). ET start is defined when the TC transitions from a warm-core, nonfrontal cyclone to a warm-core, frontal cyclone. This occurs in the cyclone phase space when the storm-motion-relative 900–600-hPa layer thickness asymmetry across the TC exceeds an empirically derived threshold of 10 m (Hart, 2001). Positive thickness asymmetry parameter values correspond to cold and/or dry air to the left of motion and warm and/or moist air to the right of motion (Evans & Hart, 2008; Hart, 2003). ET end occurs when the TC transitions from a warm-core, frontal cyclone to a cold-core, frontal cyclone. This is defined as when the 900–600-hPa thermal wind changes from positive to negative. Negative values are associated with increases in the strength of the cyclone wind field with height (Hart, 2003). Our study does not consider the small number of landfalling TCs that retain their warm core during and after transition (i.e., instant warm-seclusion), which are unable to be identified using the cyclone phase space (Sarro & Evans, 2022). Both cyclone phase space parameters are calculated over a 500-km radius from the TC center, which is the approximate length scale of North Atlantic TC outer size (Chavas et al., 2016; Schenkel et al., 2018). We use ERA5 data available at intervals between 25 and 50 hPa to compute the thickness asymmetry and thermal wind parameters.

2.6. Estimating Missing P_{min} Data

For TCs occurring before 1975, P_{min} data is missing for some IBTrACS time steps. Although P_{min} is not a required input when estimating the storm R_{max}, P_{min} does impact the modeled storm surge since the low-pressure TC center causes a small rise in ocean water level. The missing P_{min} data can be estimated using a simplification of the cyclostrophic balance equation (Knaff & Zehr, 2007):

$$P_{min} = P_{ref} - \left(\frac{V_{max}}{C}\right)^{1/n} \quad (2)$$

where C and n are empirically derived coefficients that vary with latitude and were computed in Landsea et al. (2004), Table 7.5. Alternately, gradient wind balance can be used to relate the radial profiles of pressure and azimuthal wind speed, with the wind speed profile specified by the CLE15 model. Previous work by Chavas et al. (2017) showed that the application of gradient wind balance theory can accurately predict the storm pressure deficit. A comparison of P_{min} estimated using the empirical cyclostrophic balance Equation 2 and the gradient wind balance with CLE15 wind profile yielded similar results (Figure S7 in Supporting Information S1). Since calculating P_{min} using the gradient wind balance is more computationally expensive, we opt to use the simplified cyclostrophic balance equation in place of missing data.

2.7. Hydrodynamic Modeling of TCs

To reconstruct storm surge (water level rise due to atmospheric forcing) and storm tide (total water levels including surge plus astronomical tides) from historical TCs, we develop TC wind fields from the CLE15 profile plus background wind model of N. Lin and Chavas (2012) using IBTrACS data (including intensity) and ERA5 + CLE15 size information. The wind model (CLE15 plus background wind) is coupled with the 2D, depth-integrated version of the advanced circulation (ADCIRC) hydrodynamic model (Luettich et al., 1992; Westerink et al., 1992). We utilize an unstructured computational mesh that spans the entire North Atlantic basin and has relatively high coastal resolution (~1 km). The mesh was developed and validated in Marsooli and Lin (2018). We also incorporate forcing from eight tidal constituents (K1, K2, M2, N2, O1, P1,Q1, and S2), which are estimated from the global model of ocean tides TPXO8-ATLAS (Egbert & Erofeeva, 2002). Recently, Wang et al. (2022a) showed more accurate estimates of peak storm tides in ADCIRC when it was coupled to the CLE15 model compared to the Holland wind model. Based on the track, intensity and size time histories of each TC, ADCIRC simulates peak storm tides along the US Atlantic and Gulf coasts.

We compare our storm tide and storm surge reconstructions to observed peak water level and maximum surge levels from 74 NOAA tidal gauges (https://tidesandcurrents.noaa.gov) located along the US Atlantic and Gulf coasts. Specifically, we include all active tidal gauges within 200 km of each TC track. The observed maximum storm surge is calculated at each tidal gauge by subtracting the predicted tides from the observed total water levels during the storm event. Gauges that were malfunctioning, located within river or estuaries, or where water levels were clearly impacted by freshwater discharges are excluded from the comparison. The modeled maximum storm surge is calculated by simulating storm tides within ADCIRC from wind/pressure forcing plus astronomical tides, and then subtracting an ADCIRC-simulated tide-only scenario. We divide the coastline into five regions: western Gulf of Mexico (extending until New Orleans, LA), eastern Gulf of Mexico, southeast Atlantic (until Chesapeake Bay), mid-Atlantic (until Connecticut), and New England. Tidal gauges are grouped within each region to evaluate how well the storm surge reconstructions match observations for different portions of the coast.

3. Results

3.1. Representation of TC Wind Field Within ERA5 Reanalysis

We first compare the radial structure of TC mean azimuthal wind from the ERA5 reanalysis and the QSCAT-R data. Figure 1 shows the median azimuthal-mean azimuthal wind profile across all TC time steps between 2000 and 2009 with at least tropical storm intensity from ERA5 and QSCAT-R. Although previous work found that ERA5 better resolves TCs compared to the earlier ERA-Interim (Bian et al., 2021; Dullaart et al., 2020), Figure 1 shows that the reanalysis data still largely under resolves inner TC wind speeds compared to the QSCAT-R data as expected from prior work (Schenkel & Hart, 2012; Schenkel et al., 2017). Due to limited horizontal resolution and limited sensitivity to backscatter of the scatterometer, the QSCAT-R inner core wind speeds shown in Figure 1

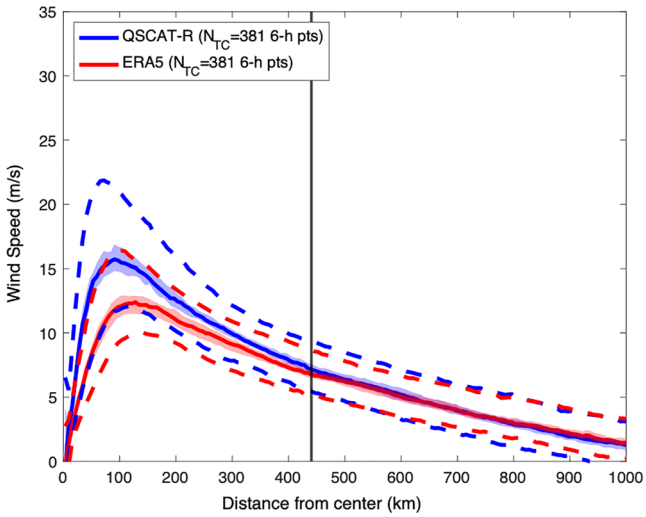

Figure 1. Median azimuthal wind profile (solid) with boot-strapped 95% confidence bounds (shaded) and inter-quartile range (dashed) for all QSCAT-R TC snapshots with V_{max} greater than 17 m/s. Black vertical line indicates the distance from TC center (in km) after which the ERA5 and QSCAT-R wind speed distributions are the same at a 5% significance level.

are likely also an underestimate of the true azimuthal-mean azimuthal wind speed. However, for wind speeds in the outer region of the storm, which is our region of interest, QSCAT-R wind speeds are highly accurate (Chavas & Vigh, 2014). The ERA5 data also overestimates R_{max} (Figure 1) likely in part because of its coarse horizontal resolution and conservative physics parameterizations (Bian et al., 2021; Schenkel et al., 2017). However, Figure 1 also shows that ERA5 represents the outer TC wind field accurately compared to QSCAT-R (Bian et al., 2021). For $r > 440$ km, where 440 km is close to the median r6 value based on QSCAT-R (Bian et al., 2021), the median wind profiles from the two data sets converge, and a Kolmogorov-Smirnov test at the 5% level suggests that wind speeds from both data sets at each subsequent radii come from the same distribution. The comparison of the wind profiles illustrates that ERA5 is a reasonable source for estimating features of the outer wind field.

3.2. Accuracy of Reanalysis-Derived Outer Size Metrics

After establishing that the TC outer wind profile from the ERA5 compares well to QSCAT-R, we next evaluate the accuracy of ERA5 outer size estimates. For each QSCAT-R data point and outer size metric (i.e., r_2, r_4, r_6, r_8, r_{10}, and r_{12}), we compare against the corresponding ERA5 sizes. The outer size analysis includes 381 QSCAT-R snapshots, although the size metrics are not all defined for each snapshot. Figure 2a shows boxplots of the difference between ERA5 and QSCAT-R for each size metric. Except for r_2, ERA5 slightly underestimates the outer size compared to QSCAT-R, with a larger negative bias for r_6–r_{12}. In contrast, the variability of the size estimates decreases for radii at higher wind speeds, demonstrated by the narrower interquartile ranges for r_{10} and r_{12}. The larger negative bias for r_{10} and r_{12} is due to ERA5 consistently under-predicting wind speeds for radial distances closer than 440 km (Figure 1a) as found in previous studies (Bian et al., 2021; Schenkel et al., 2017).

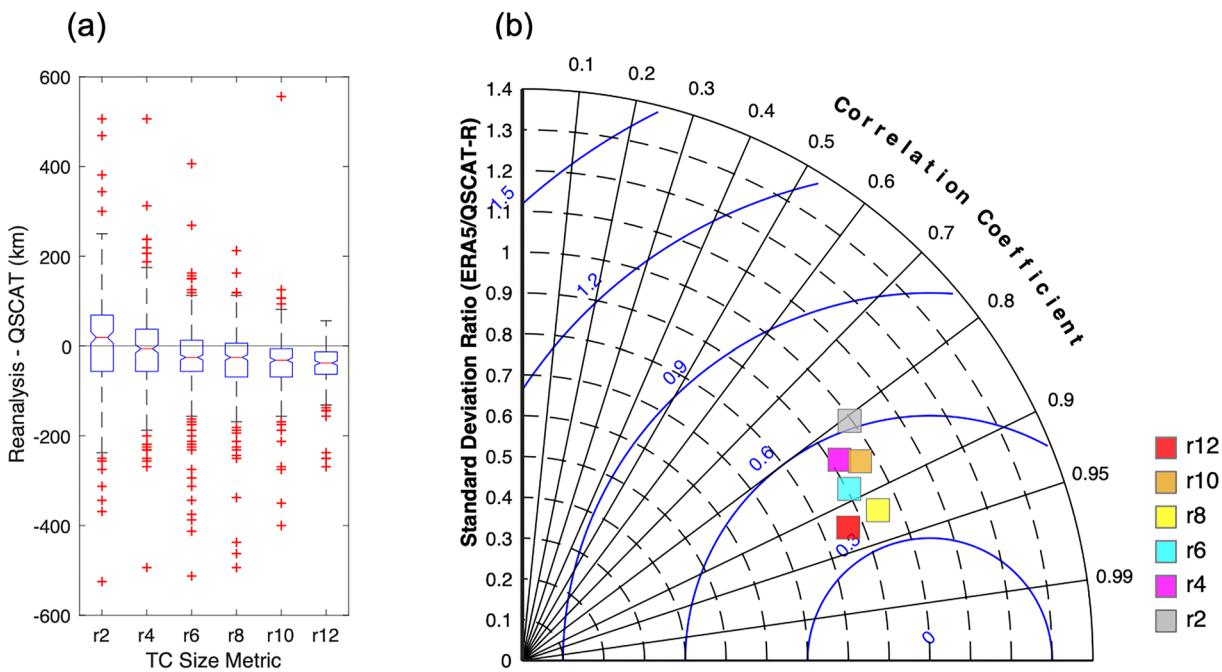

Figure 2. (a) Boxplots of outer size error of ERA5 reanalysis data compared to QSCAT-R for 381 TC snapshots at radii at which the azimuthal-mean 10-m azimuthal wind equals 12 m/s (r_{12}), 10 m/s (r_{10}), 8 m/s (r_8), 6 m/s (r_6), 4 m/s (r_4) and 2 m/s (r_2). Median of each metric shown as horizontal red line, and width of notch on each box denotes 95% uncertainty bounds of the median, calculated through bootstrapping. Red plus signs denote outliers using 1.5*IQR formula. (b) Pearson correlation (radial axis), ratio of standard deviations (y axis), and root mean square error between ERA5 and QSCAT (blue contours) for each outer size metric.

Figure 2b shows a Taylor diagram (Taylor, 2001) comparing outer size in the ERA5 versus QSCAT-R. There is high correlation between ERA5 and QSCAT-R for all size metrics, ranging from 0.8 to 0.93, with the highest correlations for r_{12} and r_8. The ratio of the standard deviations ranges from 0.8 to 1, indicating that there is less variability in the ERA5 sizes compared to QSCAT-R. The r_{12} and r_8 metrics have the lowest root-mean-square-error (RMSE), followed by r_6, r_{10}, r_4, and lastly r_2. As found in Schenkel et al. (2017), the lower correlation coefficient, higher RMSE, and higher normalized standard deviation for the r_2 metric suggests that the reanalysis data may struggle to resolve weak azimuthal-mean TC wind speeds from the environmental background wind To provide size estimates for as many time steps as possible, we still utilize the r_2 metric since the correlations are strong and normalized standard deviations are close to 1. Based on the relatively high correlation coefficients, low RMSE, and good match to QSCAT-R based outer sizes (Figure S5 in Supporting Information S1) for most other size metrics, the ERA5 reanalysis outer size estimates can be used (after bias correction) to realistically represent the outer TC wind field.

3.3. Accuracy of R_{max} Estimates

The ERA5 outer size estimates at each TC time step are bias corrected by adding the median difference between ERA5 and QSCAT-R outer size (red lines in Figure 2a) calculated for each size metric (see Section 2.2). Then, using the bias corrected outer size estimates and V_{max}* defined in Equation 1, we compute the azimuthal-mean 10-m azimuthal wind profile for each TC time step based on the CLE15 model and extract R_{max}. We compare the ERA5 + CLE15 R_{max} values against R_{max} values from IBTrACS (Figure 3) and the high-resolution HWind data set (Figure S8 in Supporting Information S1). Figure 3a shows a comparison of storm-averaged R_{max} for each TC between 2004 and 2020 for the duration of time when the TC is at least 100 km away from land and has intensity >17.5 m/s. Figures 3b–3e show a comparison of all 6-hr time steps between 2004 and 2020 with intensity >17.5 m/s and a distance to land of at least 100 km. Similarly, Figure S8 in Supporting Information S1 shows the same comparison for TC snapshots taken from HWind, while Figure S9 in Supporting Information S1 shows our calculated R_{max} compared to IBTrACS for time steps when each TC is less than 50 km from land. The HWind R_{max} comparison illustrates that the model performs well overall: the RMSE is 31 km and the mean bias is only 0.3 km. Apart from a couple tropical storm intensity outliers, the vast majority of TC snapshots in Figure S8 in Supporting Information S1 are clustered around the 1:1 line. The performance for TC time points when the storm is within 50 km of land (Figure S9 in Supporting Information S1) is lower than the storm-averaged or HWind-based performance, which is expected given that we assume no change in outer size once the TC is close to making landfall. Despite this assumption, the RMSE and mean bias (32.8 and 5.1 km, respectively) are still relatively small for TCs close to land.

3.3.1. Storm-Averaged Performance

Figure 3a shows a comparison between storm averaged R_{max} using ERA5 + CLE15 and IBTrACS. R_{max} performance is quantified using three metrics: the RMSE, mean bias, and Willmott skill (Willmott, 1981), which quantifies the degree of agreement between modeled and observed data and ranges from 0 (complete disagreement) to 1 (complete agreement). The overall storm-averaged performance is relatively good, with a Willmott skill of 0.85 and average bias of −2.2 km. The variability in the difference between ERA5 + CLE15 and IBTrACS increases with increasing R_{max}, suggesting that there is higher uncertainty for large R_{max} values. Additionally, the ERA5 + CLE15 approach performs better in terms of storm averaged R_{max} for hurricane strength (>33 m/s) storms (red and magenta points) compared to tropical storm intensity (<33 m/s) events (green points), which tend to have larger R_{max} values. The lower ERA5 + CLE15 performance for tropical storm intensity TCs could also be due to challenges extracting reanalysis outer size estimates from weak, less organized storms and CLE15's potential underestimation of R_{max} for large, weak storms (Chavas & Lin, 2016).

To measure the uncertainty associated with the ERA5 + CLE15 R_{max} estimates, we develop a low and high estimate in addition to the modeled R_{max}. We first calculate the percent difference between the IBTrACS and ERA5 + CLE15 storm averaged R_{max} values, which has a mean of approximately 0%. Then we scale all the R_{max} values up and down by one standard deviation of the percent difference to get the high and low estimates, respectively. Using this procedure, the low-high estimates overlap with the IBTrACS values for 68% of storms (close to ± one standard deviation range of a normal distribution) shown in Figure 3a.

3.3.2. Performance for Low-Latitude TCs

Figure 3b shows the comparison between ERA5 + CLE15 and IBTrACS R_{max} at each time step where a TC is below 30°N latitude. The ERA5 + CLE15 approach performs well for low latitude TCs, with a mean bias of only

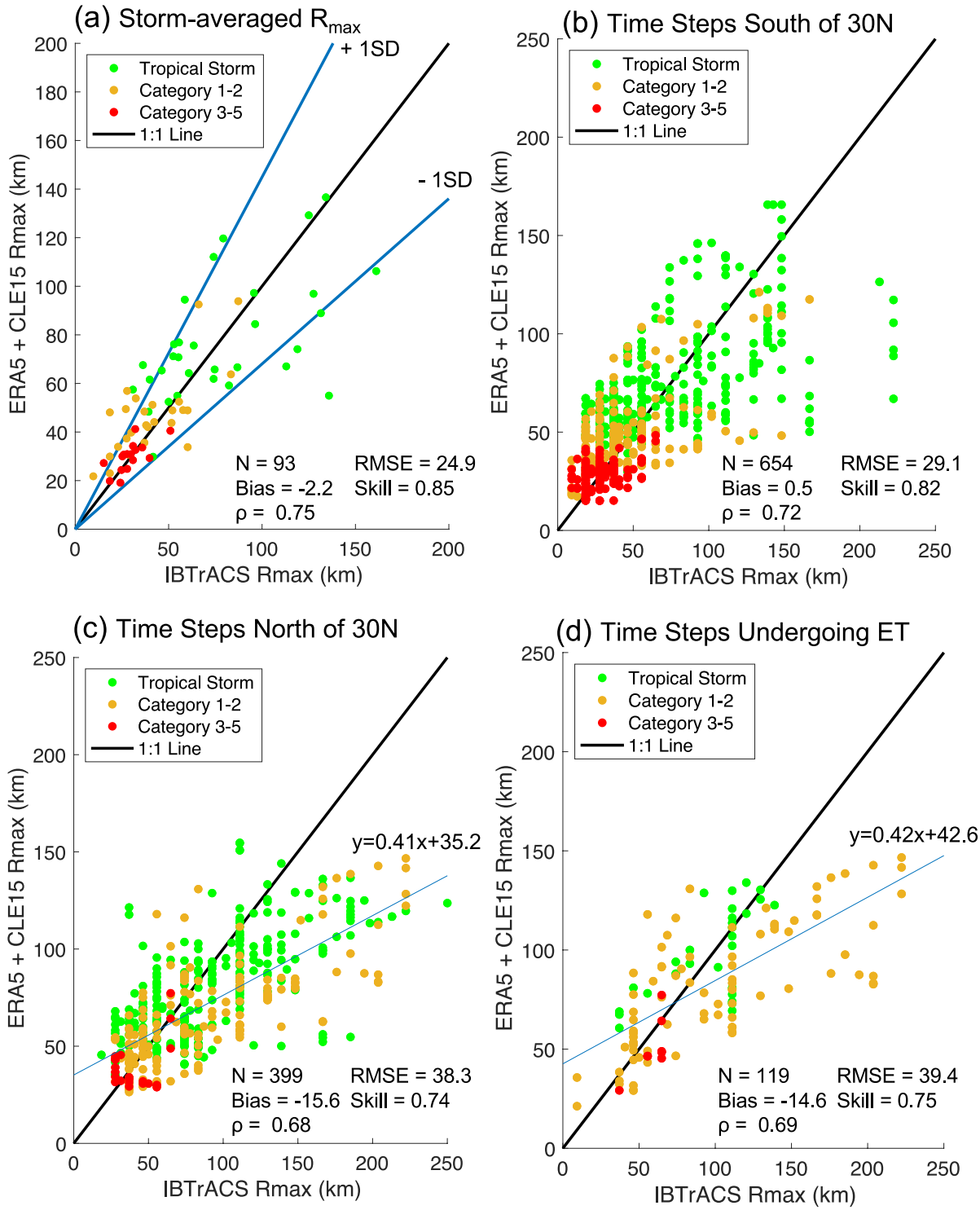

Figure 3. (a) Comparison between storm-averaged R_{max} using ERA5 outer size and CLE15 wind profile (ERA5 + CLE15) and IBTrACS Rmax for TCs where V_{max} is greater than 17 m/s. Points are colored by their Saffir-Simpson category. (b) Same as in (a) except using each 6-hr TC time step for TCs below 30° latitude, (c) same as in (b) but for TC time steps above 30° north latitude, (d) same as in (c) but for extra-tropical transitioning (ET) time steps, where ET is defined according to the cyclone phase space (Hart, 2003).

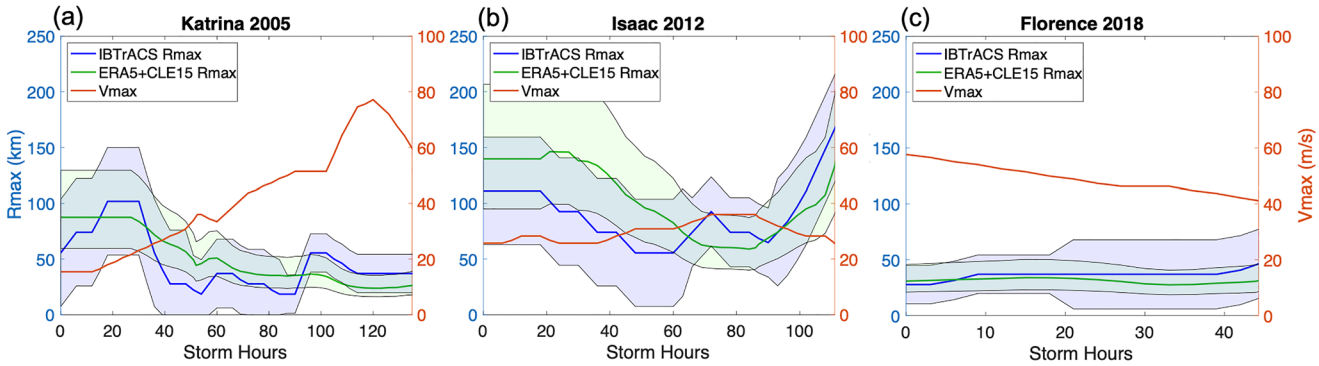

Figure 4. Evolution of IBTrACS R_{max} (blue) and ERA5 + CLE15 R_{max} (green) until the storm makes landfall, with uncertainty bounds (shaded area), and V_{max} (orange) for several major historical TCs occurring below 30°N: (a) Katrina 2005, (b) Isaac 2012, (c) Florence 2018. ERA5 + CLE15 uncertainty bounds are based on one standard deviation (Section 3.3.1) and IBTrACS uncertainty bounds are based on mean absolute error (MAE) as estimated by NHC.

0.5 km and RMSE of 29.1 km. There are a few very large, weak TCs occurring below 30° N that are underestimated by ERA5 + CLE15, and a few category 1–2 TC time steps that are also underestimated. However, most TC time steps occurring below 30°N correlate well with the IBTrACS R_{max} and fall within the IBTrACS uncertainty bounds.

To further illustrate the performance of the modeled R_{max} values at low latitudes, Figure 4 shows the temporal evolution of R_{max} until landfall (where the plots terminate) based on ERA5 + CLE15 (green) and IBTrACS R_{max} (blue) for three hurricanes that encompass a wide range of R_{max} evolution: (a) Katrina (2005), (b) Isaac (2012), and (c) Florence (2018). The model-based (standard deviation) and IBTrACS (MAE) R_{max} uncertainty ranges are also shown on each plot as shaded regions. For Isaac and Florence, the temporal evolution of modeled R_{max} tracks well with IBTrACS, as the ERA5 + CLE15 approach is able to capture the life cycle of TC size evolution. For Katrina, there is an increase in R_{max} occurring around hour 90 that was likely associated with an eyewall replacement cycle (Knabb et al., 2005), which is underestimated by ERA5 + CLE15. Across all three storms the ERA5 + CLE15 R_{max} values fall within the IBTrACS uncertainty bounds for the vast majority of time steps. Additionally, in most cases the IBTrACS values also fall within the ERA5 + CLE15 uncertainty range. In the case of Isaac, the model initially overestimates R_{max}, but the ERA5 + CLE15 and IBTrACS values converge as the storm intensifies. The examples shown in Figure 4 demonstrate that the ERA5 + CLE15 R_{max} values can realistically reproduce TC size evolution for landfalling storms.

3.3.3. Performance at Mid-Latitudes and for ET Storms

In contrast to the good performance at low latitudes, the performance of ERA5 + CLE15 is not as good for mid-high latitude storms (Figure 3c) where the model tends to underestimate R_{max} for large storms, resulting in a mean bias of −15.6 km. The performance of ERA5 + CLE15 is also not as good for ET time steps (Figure 3d), where ET time points are identified based on the cyclone phase space methodology (Section 2.5). As shown in Figures 3c and 3d, the majority of midlatitude hurricane time steps (red points) whose sizes are underestimated by ERA5 + CLE15 were also undergoing ET. ET often results in an expansion and asymmetric evolution of the wind field (Evans & Hart, 2008; Hart & Evans, 2001; Jones et al., 2003), causing an increase in R_{max} (Evans & Hart, 2008; Evans et al., 2017; Halverson & Rabenhorst, 2013) that is demonstrated by the large R_{max} for category 1–2 storms shown in Figure 3d. ET dynamics are not explicitly captured by the ERA5 + CLE15 approach since the CLE15 wind profile is based on the angular momentum distribution of a mature TC. Still, ET wind field expansion is partially accounted for in the ERA5 + CLE15 R_{max} estimates: decreasing storm intensity and increasing latitude, both of which are associated with ET, yields increased R_{max} estimates from the CLE15 model and theory (Chavas & Knaff, 2022).

Figure 5 shows the ERA5 + CLE15 R_{max} (green) and IBTrACS R_{max} (blue) evolution for three TCs reaching the mid latitudes where ERA5 + CLE15 does not perform as well: (a) Sandy (2012), (b) Jose (2017) and (c) Dorian (2019), where the vertical red line on each plot indicates ET start and the plot terminates either when the TC makes landfall or completes ET. In Sandy's case, the R_{max} had already begun expanding rapidly before ET started (according to the phase space criteria) as it transitioned from a TC into a warm-seclusion extratropical cyclone

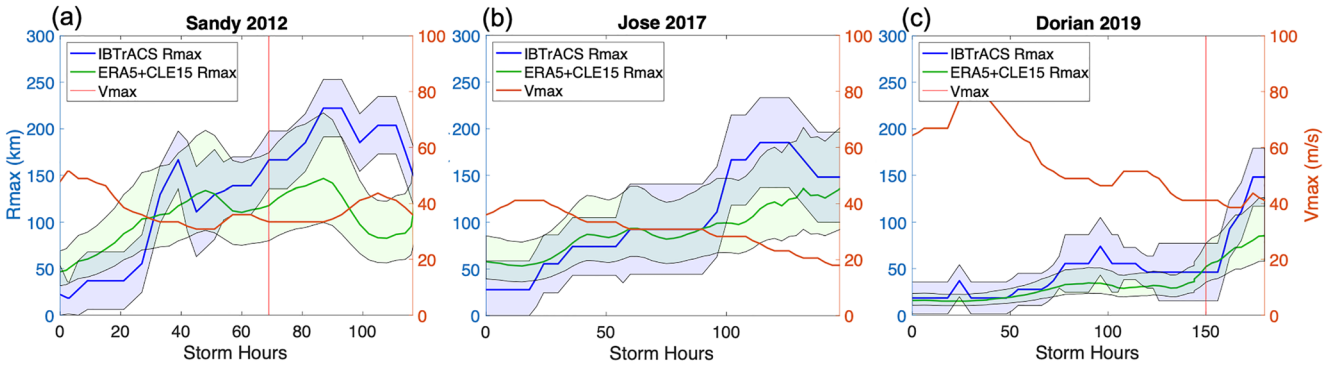

Figure 5. Evolution of IBTrACS R_{max} (blue) and ERA5 + CLE15 R_{max} (green) with uncertainty bounds (shaded area), and V_{max} (orange) for several major historical TCs reaching above 30 N: (a) Sandy (2012), (b) Jose (2017), and (c) Dorian (2019). ERA5 + CLE15 uncertainty bounds are based on one standard deviation (Section 3c.1) and IBTrACS uncertainty bounds are based on mean absolute error as estimated by NHC. Vertical red line indicates time when extra-tropical transition (ET) begins according to the cyclone phase space and plots terminate when TC makes landfall or completes ET.

(ETC) that had both tropical (warm core) and extra-tropical (frontal structure) features (Galarneau et al., 2013; Halverson & Rabenhorst, 2013). However, landfall of warm-seclusion ETCs is rare in the historical record (Sarro & Evans, 2022). ERA5 + CLE15 generally captures Sandy's R_{max} evolution until ET begins, at which point the IBTrACS R_{max} increases at a much faster rate than the model predicts, demonstrating that ERA5 + CLE15 can capture some size expansion during ET but not completely. Similarly, during Dorian the modeled R_{max} expands once ET begins (Figure 5c). However, the IBTrACS R_{max} expanded at a faster rate during ET than was predicted by the model. Hurricane Jose (Figure 5b) did not undergo ET according to the phase space criteria, but as the storm moved north it acquired some extra-tropical characteristics, which caused an increase in R_{max} (Berg, 2018).

The ERA5 + CLE15 R_{max} estimates for midlatitude and ET storms cannot be corrected using a simple linear fit against the IBTrACS data. Figures 3c and 3d show that ERA5 + CLE15 performs well for TC time steps where R_{max} is less than roughly 120 km (see small storms clustered around the 1:1 line) but tends to largely underestimate R_{max} for larger storms (see divergence from 1:1 line for large storms). For example, the mean bias for mid-latitude (ET) storms with R_{max} smaller than 120 km is only −2 km (−2.6 km), but is −60 km (−60 km) for mid-latitude (ET) storms larger than 120 km. R_{max} is generally calculated as the location of highest wind speed occurring anywhere in the storm (compared to location of highest azimuthal-mean wind speed) and ET storms may have non-negligible asymmetry. Therefore, the uncertainty associated with the IBTrACS R_{max} values may be larger for ET storms. Despite the larger negative bias and higher uncertainty for large ET storms, the ERA5 + CLE15 approach produces reasonable TC size estimates that can be utilized for hazard analysis. Storm surges along the Mid-Atlantic and New England coastlines are less sensitive to R_{max} compared to other coastal regions (see Section 3.4) and errors in R_{max} during ET do not result in large errors in peak storm tides or surges (with the exception of Hurricane Sandy) as shown in the next section (see Figure 6 and Figure S10 in Supporting Information S1) Therefore, we use un-adjusted ERA5 + CLE15 R_{max} estimates in conjunction with the low-high ranges developed in Section 3.3.1.

3.4. Modeled and Observed Storm Tides and Surges

In addition to developing a record of historical TC sizes, the second goal of our study is to develop a spatio-temporally continuous database of peak TC storm tides and storm surges. By incorporating TCs from 1950 to 1987, we reconstruct storm tides for an additional 227 events compared to previous databases (e.g., Marsooli & Lin, 2018) beginning in 1988. We simulate peak storm tide and surge (storm tide minus astronomical tide) using the ERA5 + CLE15 size estimates and the ADCIRC hydrodynamic model (forced with the CLE15 wind model) and compare our modeled maximum storm tide/surge against observed maximum water level and maximum storm surge from 74 tidal gauges along the US coastline. Figure 6 (Figure S10 in Supporting Information S1) shows scatterplots of observed and modeled peak storm tide (surge) and associated performance metrics at each active tidal gauge within each coastline region, where the regions are defined in Figure 8. Each point is colored based on the decade in which the storm occurred. Across all regions of the coastline, the reconstructed storm tides and storm surges match relatively well against observed water levels, with skill scores ranging from 0.89 to

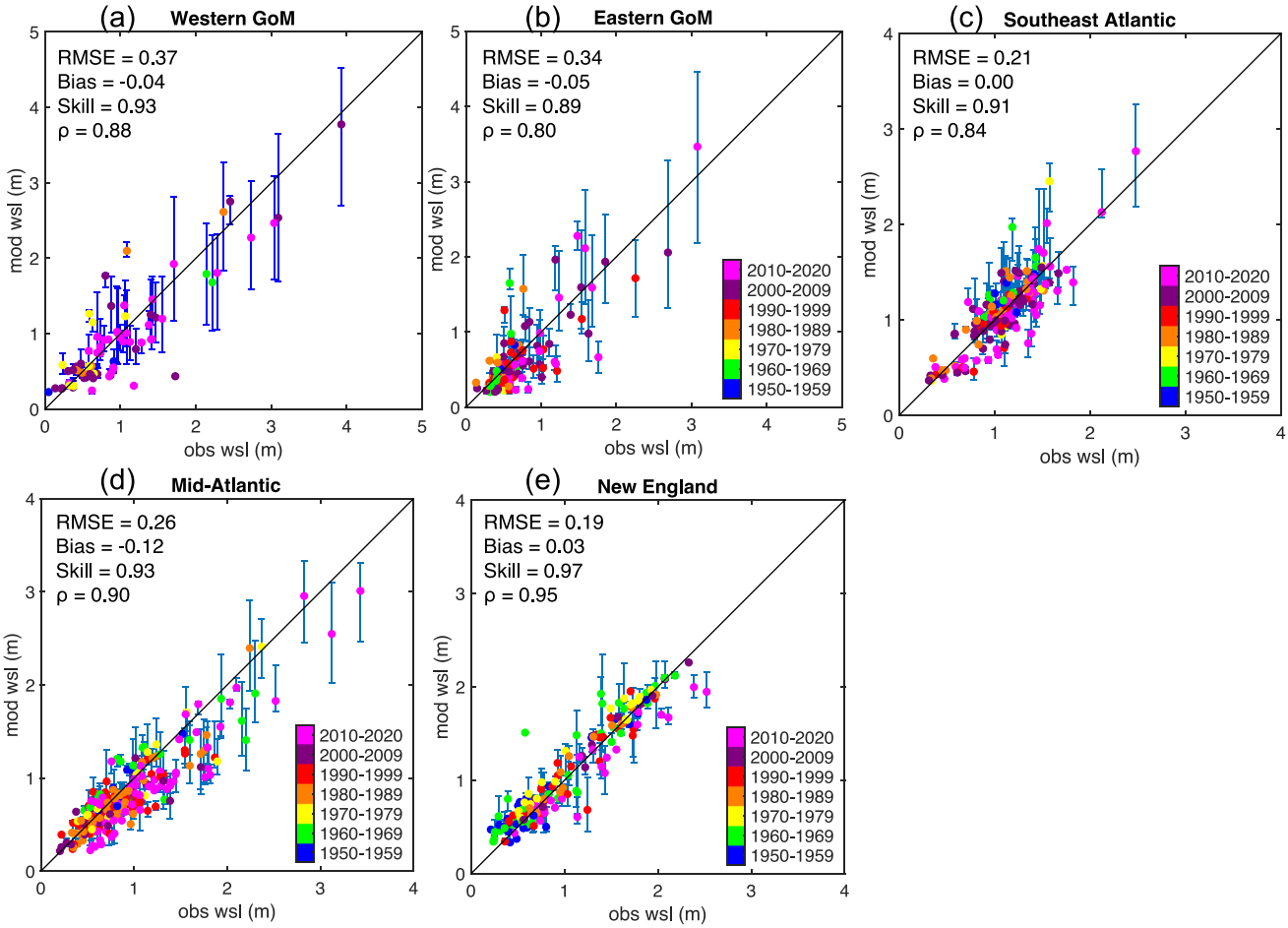

Figure 6. Comparison of modeled peak storm tides and observed peak storm tides for all historical TCs between 1950 and 2020 grouped into five regions: (a) Western Gulf of Mexico, (b) Eastern Gulf of Mexico, (c) Southeast Atlantic, (d) Mid-Atlantic, and (e) New England. Points are colored by decade and depict associated error bars (one standard deviation of R_{max}). Performance metrics are root-mean-square-error, mean bias, Willmott skill, and Pearson correlation (ρ).

0.97 for storm tide and 0.82–0.94 for storm surge. The mean bias ranges from −0.12–0.03 m for storm tide and −0.19–−0.02 m for storm surge (where negative bias indicates model under prediction). The model performance is higher for peak storm tide compared to storm surge since the storm tide includes the effect of astronomical tides, which are well-simulated by the ADCIRC model. Nevertheless, the maximum storm surge comparison (Figure S10 in Supporting Information S1) demonstrates that the modeling approach can still represent surge severity with relatively high skill and high correlation compared to observed surge at most gauge locations. Both the western and eastern Gulf of Mexico (GoM) have larger RMSE for storm tide and surge estimates compared to locations along the Atlantic coast. The larger RMSE in the GoM is due to the coastline configuration and wide continental shelf, which causes storm tides to be highly sensitive to TC size in addition to TC intensity (Irish et al., 2008). Along the southeast Atlantic, there is lower RMSE and bias compared to the GoM, but the skill (0.82) and Pearson correlation (0.69) for storm surge is the lowest of any region. Here, high surge events are generally well-captured, but there is more variability in the performance for small surge events. In the middle Atlantic, there is high correlation (0.90 for storm tide and 0.89 for storm surge) and high skill (0.93 for both) in matching observed water levels. High surge events are mostly modeled accurately (with the exception of one gauge during Hurricane Sandy; see Figure S10 in Supporting Information S1). The modeled and simulated storm tides and surges also match very closely in the New England region because the large tidal amplitudes modulate the effect of the wind-driven storm surge (Arns et al., 2020). Despite these differences in performance across different coastal regions, the comparisons shown in Figure 6 and Figure S10 in Supporting Information S1 demonstrate that the models perform well for both early storms (1950–1979; see performance in Figure S11 of the Supporting Information S1) and more recent storms (1980–2020).

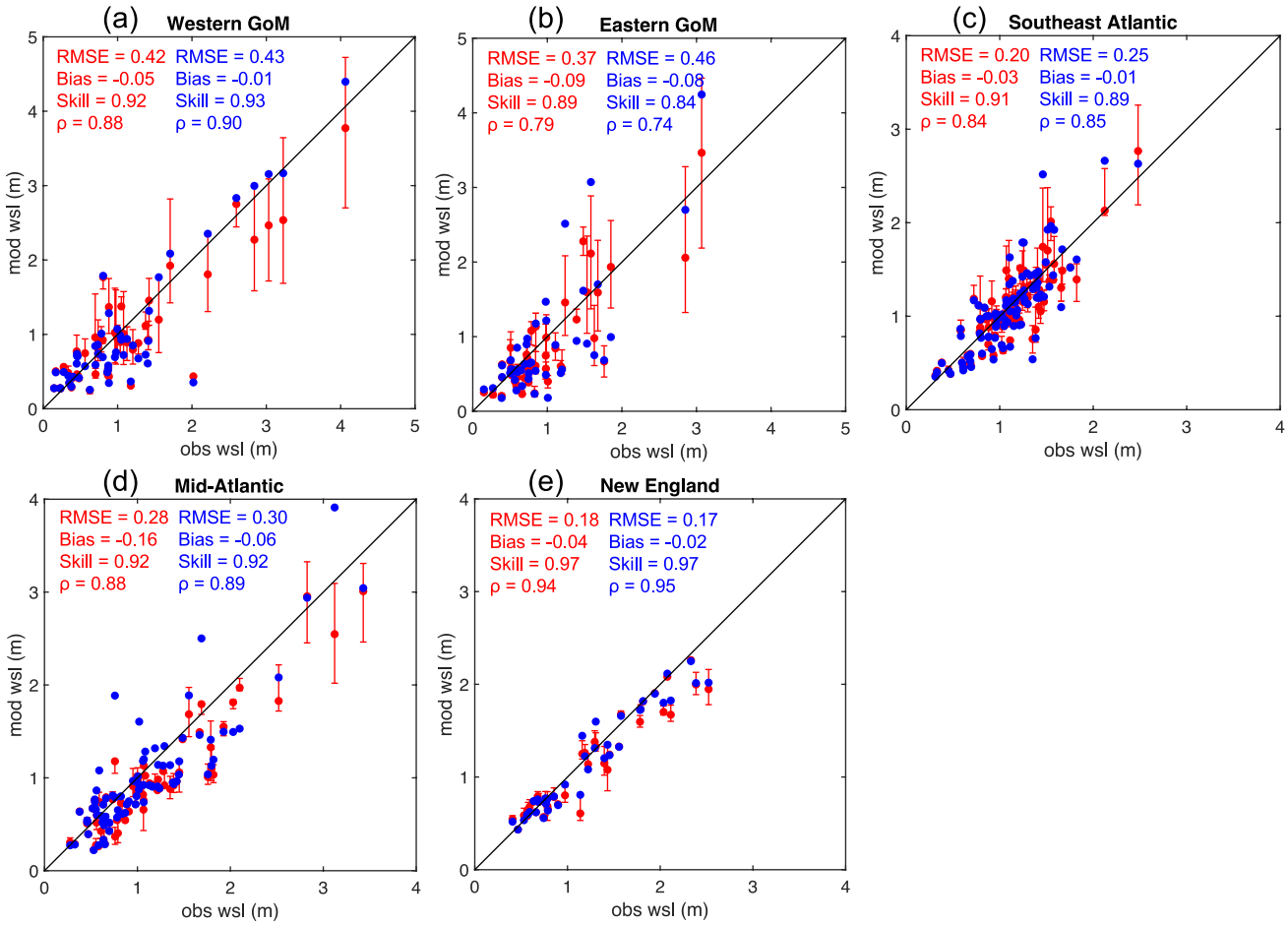

Figure 7. Comparison of modeled peak storm tides and observed peak storm tides for all historical TCs between 2004 and 2020 grouped into five regions: (a) Western Gulf of Mexico, (b) Eastern Gulf of Mexico, (c) Southeast Atlantic, (d) Mid-Atlantic, and (e) New England. Red points were modeled using ERA5 + CLE15 TC size and show associated error bars (±one standard deviation of R_{max}). Blue points were modeled used IBTrACS size data.

The errors between the observed and modeled storm tides and surges could stem from multiple sources including uncertainty in R_{max}, TC position, or intensity from IBTrACS (Landsea & Franklin, 2013). Wave impacts, or errors stemming from the hydrodynamic mesh and/or physics of the ADCIRC model may also contribute to storm surge errors. Additionally, the parametric wind and pressure models used to represent the TC within ADCIRC may not match perfectly against the true TC wind/pressure fields. Therefore, to isolate the impact of the ERA5 + CLE15 R_{max} estimate procedure, Figure 7 (Figure S12 in Supporting Information S1) shows similar comparisons of modeled and observed peak storm tide (surge) from 2004 to 2020, where red dots are modeled using ERA5 + CLE15 estimated sizes and blue dots are based on the IBTrACS size. The difference in performance between ERA5 + CLE15 storm tides and surges and IBTrACS storm tides and surges is small in the western GoM and New England regions. In the eastern GoM, the performance is slightly better using the ERA5 + CLE15 estimates rather than the IBTrACS R_{max}, while in the southeast and middle Atlantic there is a moderate improvement in performance when using IBTrACS size rather than ERA5 + CLE15. For all regions the ERA5 + CLE15 storm tides and surges have a larger negative bias compared to the IBTrACS storm tides, but the high storm tide/surge events are similarly well captured by ERA5 + CLE15 (except one gauge during Sandy). The mean storm tide (surge) bias for the mid-Atlantic is −0.16 m (−0.21 m) when using ERA5 + CLE15 to estimate R_{max}, compared to −0.06 m (−0.11 m) when using the IBTrACS R_{max}. The slight underestimation of storm tides caused by using ERA5 + CLE15 storm size estimates could be due to the CLE15 model's underestimation of R_{max} at mid-high latitudes and for ET storms (discussed in Section 3.3). Nevertheless, Figure 7 and Figure S12 in Supporting Information S1 shows that using ERA5 + CLE15 to estimate the storm size does not result in much worse storm tide or surge predictions compared to using the IBTrACS data. The storm tide performance

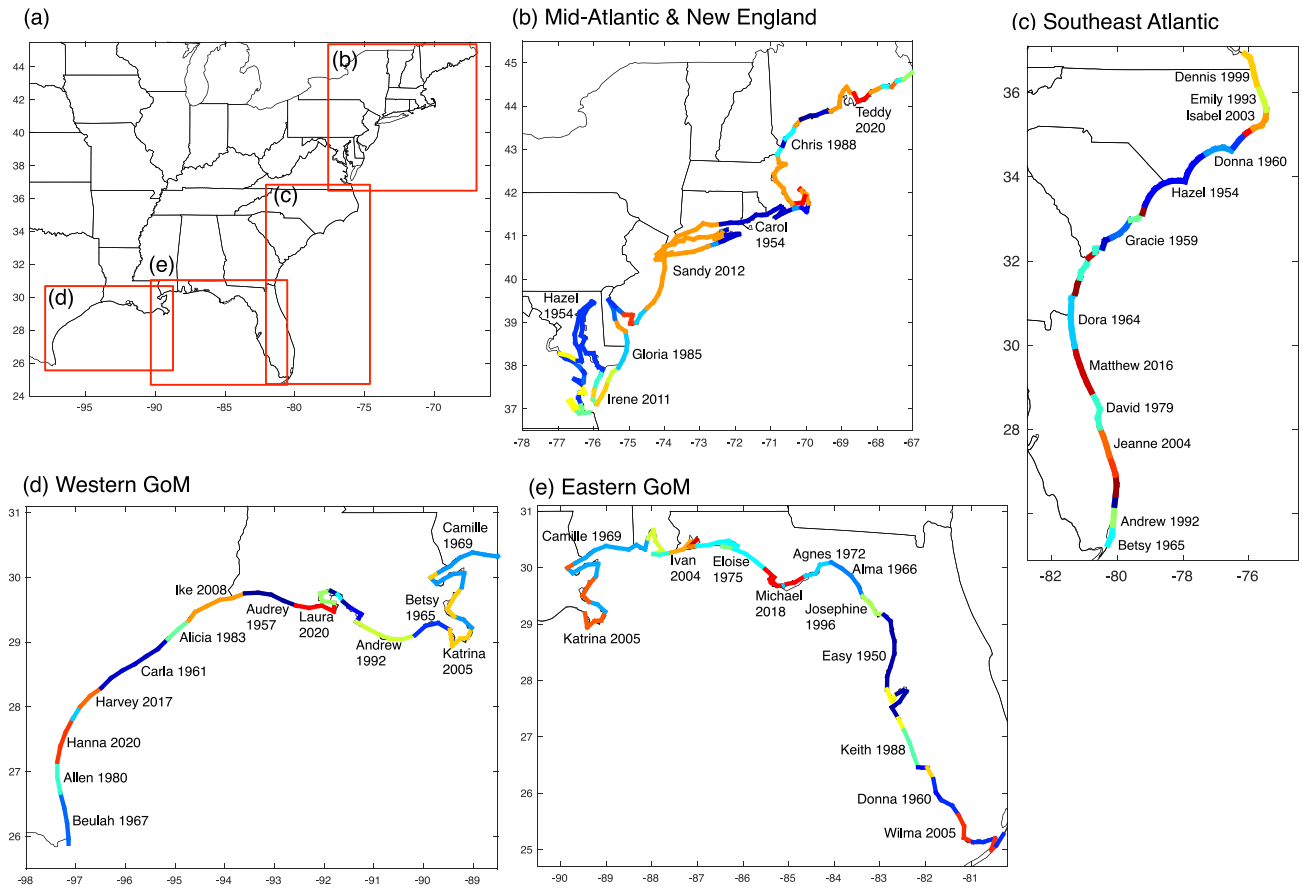

Figure 8. Storms that produced maximum modeled storm tides with different colors showing the areal extent of maximum storm tides for each storm across each region of the coastline (a): (b) Mid-Atlantic and New England, (c) Southeast Atlantic, (d) Western Gulf of Mexico, (e) Eastern Gulf of Mexico.

metrics obtained by using the ERA5 + CLE15 R_{max} estimates are also similar to the performance metrics reported in Marsooli and Lin (2018), which utilized the same basin-scale mesh as this study and modeled storm tides for TCs from 1988 to 2015 using Extended Best Track (Demuth et al., 2006) R_{max}. Modeled peak storm tides from Marsooli and Lin (2018) had an average RMSE, bias, and Willmott skill of 0.31, −0.04, and 0.90, respectively. In comparison, we report an average RMSE, bias, and Willmott skill of 0.29, −0.07, and 0.92 for all TCs from 2004 to 2020.

3.5. Impact of TCs From 1950 to 1988 on Storm Surge Hazard

To demonstrate the potential value of our reconstructions, we investigate how storm tides from TCs occurring between 1950 and 1987 can provide additional insight about coastal storm surge hazard. We model storm tides from 467 landfalling TCs, 227 of which occurred before 1988. Figure 8 shows which TCs caused the largest peak storm tides along different regions of the coastline. Along the mid-Atlantic and New England, Hurricane Sandy (2012) caused the highest storm tides for a large portion of the coastline. However, Hurricanes Hazel (1954) and Carol (1954) caused the most extreme storm surges in the Chesapeake Bay and Rhode Island, respectively. Hazel made landfall near the South/North Carolina boarder as a category 4 storm, and caused the highest storm tide levels along northern South Carolina and southern North Carolina, and in the Chesapeake Bay. Hazel's intense winds prior to landfall funneled large amounts of water into the Chesapeake Bay and the resulting storm surge coincided with high tide, driving water levels even higher.

In the southeast Atlantic (Figure 8c) there are many storms before 1988 that caused the highest storm tides along different portions of the coast, including Hazel (1954), Gracie (1959), Dora (1964), and David (1979). Gracie made landfall nearly perpendicular to the coast as a category 4 storm along the southern South Carolina coast,

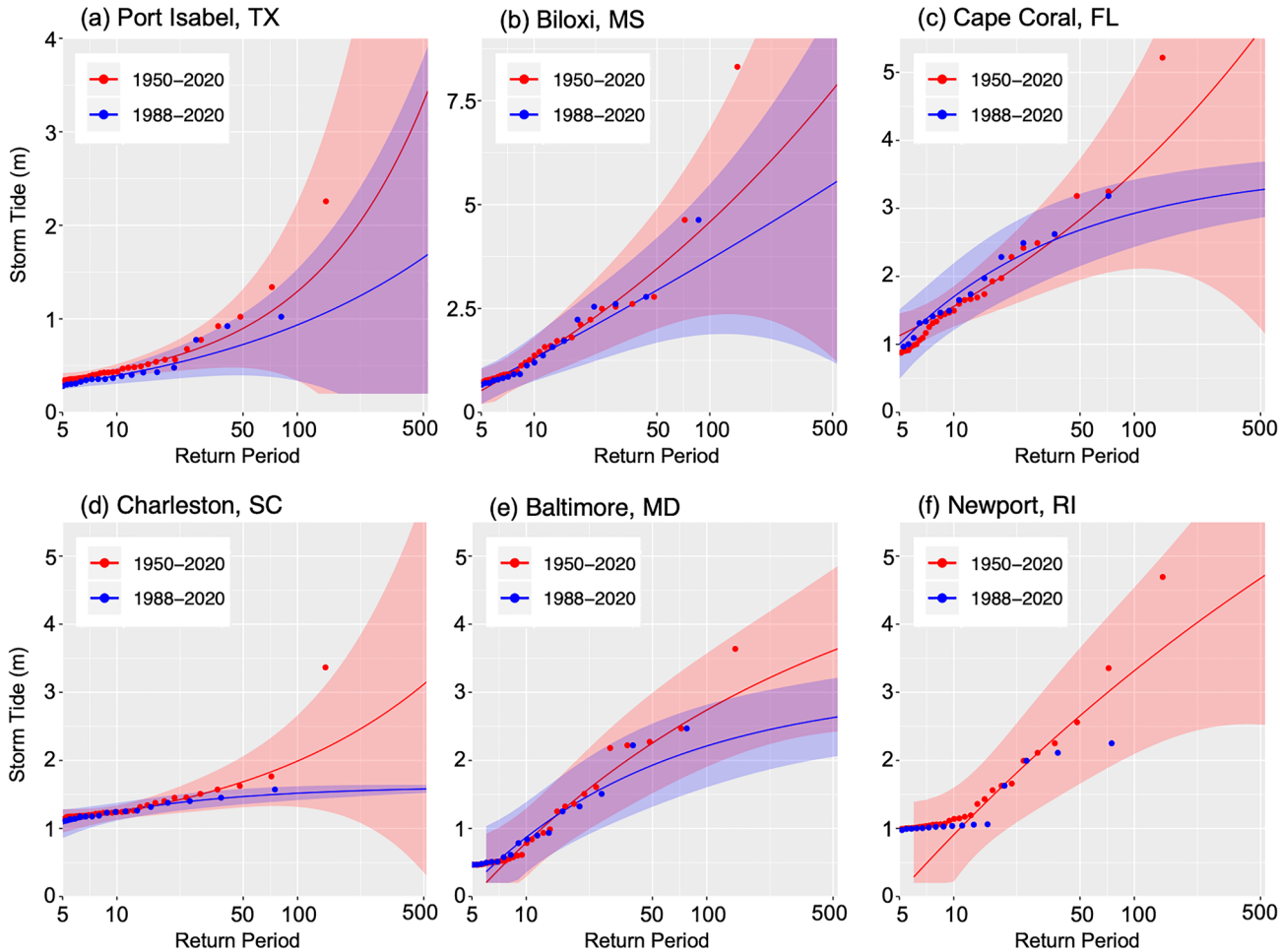

Figure 9. Storm tide return levels at select coastal locations using TCs from 1950 to 2020 (red) and using TCs from 1988 to 2020 (blue). Shading represents 95% confidence intervals and points represent individual storms.

causing widespread storm surge flooding despite arriving at low tide. In contrast, David moved parallel to the east coast of Florida as a weak hurricane, but still induced large storm tides in the Cape Canaveral region.

Similarly, along the eastern GoM (Figure 8e) Camille (1969), Easy (1950), and Donna (1960) caused extreme storm surges. Camille, which made landfall near the border of Louisiana and Mississippi, was the second most intense storm to strike the US, and caused devastating storm tides that reached up to 6–9 m along the coastline of Mississippi (ESSA, 1969; NBS, 1971). Along the western GoM, Beulah (1967) and Carla (1961) were the most devastating pre-1988 TCs. Beulah was one of the most powerful hurricanes to hit the lower Texas coast, causing widespread storm surges and coastal erosion.

While Figure 8 illustrates which TCs caused the largest storm surge impacts, it does not tell us how the incorporation of TCs from 1950 to 1987 impacts our estimates of storm surge climatology and hazard. Incorporating a larger sample size of historical TCs occurring from 1950 to present can allow additional rare, extreme storms to be captured in the modeled database, enabling better estimation of storm surge hazard. Figure 9 compares storm tide return period curves at several coastal locations derived from modeled storm tides occurring from 1950 to 2020 (red) and similar curves derived from only 1988–2020 TCs (blue). The curves in Figure 9 were calculated by fitting modeled storm tides with a generalized pareto distribution for the tail and assuming TC arrivals occur as a Poisson process (N. Lin, Emanuel et al., 2010; N. Lin, Smith, et al., 2010; N. Lin et al., 2012; Marsooli et al., 2019). The shaded regions around each return period curve represent the 95% confidence intervals calculated according to the Delta method (Coles, 2001). The locations in Figure 9 were chosen because there are significant differences between the return period curves derived from the entire data set compared to the more

recent subset of storms. The difference in the climatology of peak storm tides between the two periods (1950–2020 vs. 1988–2020) is mainly changes in the upper tail of the distribution. The differences in mean peak storm tide between 1950–2020 and 1988–2020 are negligible at each location in Figure 9, and even the difference in the 90th percentile is small at most locations. For example, at Port Isabel, TX the 90th percentile peak storm tide from 1988 to 2020 is 0.86 m and is 0.88 m from 1950 to 2020. However, for higher percentiles (or equivalently, for higher return periods) the differences become larger (see Figure 9 showing divergence of return level curves for high return periods). At Port Isabel (Figure 9a), the extreme storm surges from Beulah (1967) as well as Allen (1980) cause the 100-year storm tide estimate to increase from 0.97 to 1.28 m above mean sea level. At Biloxi, MS (Figure 9b), the extreme winds from Camille (1969) caused 8 m of storm tide, which is over 3 m higher than the second highest storm tide event (4.6 m caused by Katrina in 2005). The 100-year storm tide at Biloxi, MS based on all storms from 1950 to 2020 is 4.6 m, while the 100-year estimate for 1988-2020 storms is only 3.7 m. Hurricane Camille is the primary data point causing an increase in 100-year storm tide: the incorporation of Camille's storm tide alone increases the 100-year storm tide to 4.4 m.

Incorporating a larger sample size of events can also impact the estimated shape of the storm tide distribution at some locations. For example, at Cape Coral (Figure 9c) and Charleston (Figure 9d) incorporating storm tides from 1950 to 1987 changes the estimated tail behavior of the distribution from a bounded tail to an unbounded tail, while at Baltimore (Figure 9e) the distribution changes to a higher upper bound. Unbounded tail behavior causes the storm tide return level to increase exponentially with increasing log return period, albeit with higher uncertainty bounds as calculated through the Delta method. The return period estimates for a bounded versus unbounded distribution diverge increasingly for high storm tide values. For example, at Charleston the peak storm tide from Gracie (1959) was around 3.3 m, which is estimated as a 600-year event using the 1950–2020 return level curve. However, if we use the 1988–2020 curve, Gracie's return period would be undefined since the bounded tail distribution predicts zero probability for such a large event to occur. At Newport, RI (Figure 9f) the top three storm tide events all occurred before 1987 with the largest storm tide caused by Hurricane Carol (1954). Because TC occurrences from 1988 to 2020 at Newport are so limited, it is not possible to fit a GP distribution to the 1988–2020 data. However, by incorporating the earlier TCs, it is possible to fit the GP distribution and obtain an estimate of the 100-year storm tide, which is 3.3 m. Although multiple additional high surge events are added to the model record at each location shown in Figure 9, the additional storms from 1950 to 1988 do not add enough data to shrink the return level confidence intervals. In cases where the tail behavior changes from bounded to unbounded, the confidence intervals become larger due to higher standard errors associated with an unbounded shape parameter. Our model reconstructions may not increase the robustness of the storm tide extreme value statistics, but they may largely change maximum likelihood-based hazard estimates.

The analysis presented here illustrates how the newly reconstructed storm tides from TCs occurring in 1950–1987 can provide valuable information about storm surge hazard across the US coastline. By developing continuous maps of peak storm tides, these reconstructions can supplement sparse gauge observations and provide a more complete understanding of historical TC storm surge hazard. Similarly, the reconstructed TC size data together with track and intensity data can be used to enhance estimates of historical TC wind (Wang et al., 2022a) and rainfall, based on physical rainfall models (Feldmann et al., 2019; Xi et al., 2020; Zhu et al., 2013).

4. Discussion and Conclusions

In this study we develop a database of reconstructed historical TC sizes and storm tides/surges based on a combination of reanalysis data and physics-based modeling. Specifically, we demonstrate that the ERA5 reanalysis data can represent TC outer size with reasonable accuracy compared to observations. We then show that the physics-based CLE15 model can reasonably reproduce the TC R_{max} using Best Track intensity information and reanalysis-based outer size. Here we estimate R_{max} through a weighted average of values based on all available outer size metrics in an effort to reduce noise-induced biases that may occur when using a single outer size metric. Future work could examine the sensitivity of R_{max} to the use of different size metrics, possibly determining which outer size metric provides the most reliable R_{max} estimates. Finally, we utilize the size reconstructions to develop a data set of modeled coastal storm tides for TCs making landfall between 1950 and 2020 and demonstrate that the modeled storm tides and surges compare well against tidal gauge observations.

The TC reconstruction methodology demonstrated here can be used in a variety of future applications, including quantification of wind, surge, and rainfall hazard, as well multi-hazard assessment (Gori et al., 2022; Moftakhari

et al., 2017; Nasr et al., 2021; Song et al., 2020; Wahl et al., 2015). The TC size data generated here for the North Atlantic can also be combined with track and intensity data, and high-resolution ocean and atmosphere models to conduct detailed hindcast analysis of extreme winds, rainfall and storm surges (N. Lin, Emanuel et al., 2010; N. Lin, Smith, et al., 2010) for pre-1988 TCs impacting the US coastline. The reconstructed size and storm tide data could also be used as input data for TC impact models (Hatzikyriakou et al., 2016; Nofal et al., 2021; Pilkington & Mahmoud, 2016) to reconstruct economic losses from historical TCs and conduct TC risk analysis. The ERA5 + CLE15 approach could also be applied to reconstruct sizes in other ocean basins where TC data may be more limited or discontinuous (Knaff et al., 2018; Kossin et al., 2013). The CLE15 model can be combined with climatological mean values of outer size (Chavas & Emanuel, 2010; Chavas et al., 2016) to reconstruct TC wind fields and storm surges for storms occurring before 1950, similar to the approach implemented in N. Lin et al. (2014). Finally, the approach described here could be utilized with output from general circulation models (GCMs) to evaluate changes in TC climatology and hazards resulting from different climate warming scenarios.

The TC size and storm tide reconstructions developed here may be impacted by limitations and uncertainties stemming from the ERA5 reanalysis data (discussed in Sections 2.2 and 3.2), CLE15 wind model (Section 3.3), and hydrodynamic model and mesh (Section 3.4). Although there is higher uncertainty associated with the use of ERA5 to represent 1950–1979 TCs, storm tide and surge modeling results suggest that our approach can well-capture peak water levels induced by early TCs. The ERA5 + CLE15 approach has lower performance for ET storms (Figure 3d), which are often characterized by asymmetric evolution of the storm wind field that cannot easily be captured by idealized wind models. Nevertheless, our modeling framework still accurately simulates peak storm tides along the Mid-Atlantic and New England coastlines (Figures 6d and 6e). Moreover, the ERA5 + CLE15 approach performs with high skill and near-zero bias for TC time steps below 30°N (Figure 3b) and on a storm-averaged basis (Figure 3a), suggesting that our size reconstructions can reasonably represent pre-1988 TCs.

Data Availability Statement

All data utilized in this study come from publicly available repositories (cited in the manuscript). All data generated from this study, including estimated TC sizes and modeled storm tides are published in Gori and Lin (2022) within the NSF DesignSafe-CI and can be freely accessed online (https://www.designsafe-ci.org/data/browser/public/designsafe.storage.published/PRJ-3777). The code for the CLE15 wind model is published in Chavas (2022) and can be freely accessed through the Purdue University Research Repository (https://purr.purdue.edu/publications/4066/1). The code for implementing the CLE15 wind model within ADCIRC is published in Wang et al. (2022b) within the NSF DesignSafe-CI and can be freely accessed online (https://doi.org/10.17603/ds2-xd0r-bk81).

Acknowledgments
A.G. was supported by a National Defense Science & Engineering Graduate (NDSEG) fellowship from the US Department of Defense. N.L. was supported by National Science Foundation (NSF) Grant 1652448. D.C. was supported by NSF Grant AGS 1945113.

References

Arns, A., Wahl, T., Wolff, C., Vafeidis, A. T., Haigh, I. D., Woodworth, P., et al. (2020). Non-linear interaction modulates global extreme sea levels, coastal flood exposure, and impacts. *Nature Communications*, *11*, 1–9. https://doi.org/10.1038/s41467-020-15752-5

Bass, B., Irza, J. N., Proft, J., Bedient, P., & Dawson, C. (2017). Fidelity of the integrated kinetic energy factor as an indicator of storm surge impacts. *Natural Hazards*, *85*(1), 575–595. https://doi.org/10.1007/s11069-016-2587-3

Berg, R. (2018). National hurricane center tropical cyclone report. *Hurricane Jose*.

Beven, J. L., Avila, L. A., Blake, E. S., Brown, D. P., Franklin, J. L., Knabb, R. D., et al. (2008). Atlantic hurricane season of 2005. *Monthly Weather Review*, *136*(3), 1109–1173. https://doi.org/10.1175/2007MWR2074.1

Bian, G. F., Nie, G. Z., & Qiu, X. (2021). How well is outer tropical cyclone size represented in the ERA5 reanalysis dataset? *Atmospheric Research*, *249*, 105339. https://doi.org/10.1016/j.atmosres.2020.105339

Blake, E. S., Kimberlain, T., Berg, R., Cangialosi, J., & Beven, J., II. (2013). Tropical cyclone report: Hurricane Sandy.

Blake, E. S., & Zelinsky, D. A. (2017). *Tropical cyclone report*. Hurricane Harvey.

Chavas, D. R. (2022). *Code for tropical cyclone wind profile model of Chavas et al (2015, JAS)*. Purdue University Research Repository. https://doi.org/10.4231/CZ4P-D448

Chavas, D. R., & Emanuel, K. A. (2010). A QuikSCAT climatology of tropical cyclone size. *Geophysical Research Letters*, *37*(18), 10–13. https://doi.org/10.1029/2010GL044558

Chavas, D. R., & Knaff, J. A. (2022). A simple model for predicting the hurricane radius of maximum wind from outer size. *Weather Forecast Accepted*, 1–20.

Chavas, D. R., & Lin, N. (2016). A model for the complete radial structure of the tropical cyclone wind field. Part II: Wind field variability. *Journal of the Atmospheric Sciences*, *73*(8), 3093–3113. https://doi.org/10.1175/JAS-D-15-0185.1

Chavas, D. R., Lin, N., Dong, W., & Lin, Y. (2016). Observed tropical cyclone size revisited. *Journal of Climate*, *29*(8), 2923–2939. https://doi.org/10.1175/JCLI-D-15-0731.1

Chavas, D. R., Lin, N., & Emanuel, K. (2015). A model for the complete radial structure of the tropical cyclone wind field. Part I: Comparison with observed structure. *Journal of the Atmospheric Sciences*, *72*(9), 3647–3662. https://doi.org/10.1175/JAS-D-15-0014.1

Chavas, D. R., Reed, K. A., & Knaff, J. A. (2017). Physical understanding of the tropical cyclone wind-pressure relationship. *Nature Communications*, *8*(1), 1360. https://doi.org/10.1038/s41467-017-01546-9

Chavas, D. R., & Vigh, J. (2014). QSCAT-R: The QuikSCAT tropical cyclone radial structure dataset NCAR Tech. Note TN-513+STR.

Chen, J., & Chavas, D. R. (2020). The transient responses of an axisymmetric tropical cyclone to instantaneous surface roughening and drying. *Journal of the Atmospheric Sciences*, *77*(8), 2807–2834. https://doi.org/10.1175/JAS-D-19-0320.1

Cline, I. (1900). Special report on the Galveston Hurricane of September. *8*, 1900.

Coles, S. (2001). *An introduction to statistical modeling of extreme values*. Springer-Verlag.

Delgado, S., Landsea, C. W., & Willoughby, H. (2018). Reanalysis of the 1954-63 Atlantic hurricane seasons. *Journal of Climate*, *31*(11), 4177–4192. https://doi.org/10.1175/JCLI-D-15-0537.s1

Demuth, J. L., DeMaria, M., & Knaff, J. A. (2006). Improvement of advanced microwave sounding unit tropical cyclone intensity and size estimation algorithms. *Journal of Applied Meteorology and Climatology*, *45*(11), 1573–1581. https://doi.org/10.1175/JAM2429.1

Done, J. M., Ge, M., Holland, G. J., Dima-West, I., Phibbs, S., Saville, G. R., & Wang, Y. (2020). Modelling global tropical cyclone wind footprints. *Natural Hazards and Earth System Sciences*, *20*(2), 567–580. https://doi.org/10.5194/nhess-20-567-2020

Dullaart, J. C. M., Muis, S., Bloemendaal, N., & Aerts, J. C. J. H. (2020). Advancing global storm surge modelling using the new ERA5 climate reanalysis. *Climate Dynamics*, *54*(1–2), 1007–1021. https://doi.org/10.1007/s00382-019-05044-0

Dullaart, J. C. M., Muis, S., Bloemendaal, N., Chertova, M. V., Couasnon, A., & Aerts, J. C. J. H. (2021). Accounting for tropical cyclones more than doubles the global population exposed to low-probability coastal flooding. *Communications Earth & Environment*, *2*, 1–11. https://doi.org/10.1038/s43247-021-00204-9

ECMWF. (2021). ERA5 back extension 1950-1978 (Preliminary version): tropical cyclones are too intense [WWW Document]. Retrieved from https://confluence.ecmwf.int/display/CKB/ERA5+back+extension+1950-1978+%28Preliminary+version%29%3A+tropical+cyclones+are+too+intense

Egbert, G. D., & Erofeeva, S. Y. (2002). Efficient inverse modeling of barotropic ocean tides. *Journal of Atmospheric and Oceanic Technology*, *19*(2), 183–204. https://doi.org/10.1175/1520-0426(2002)019<0183:EIMOBO>2.0.CO;2

Emanuel, K., & Rotunno, R. (2011). Self-stratification of tropical cyclone outflow. Part I: Implications for storm structure. *Journal of the Atmospheric Sciences*, *68*(10), 2236–2249. https://doi.org/10.1175/JAS-D-10-05024.1

ESSA. (1969). Hurricane Camille preliminary report.

Evans, C., & Hart, R. E. (2008). Analysis of the wind field evolution associated with the extratropical transition of Bonnie (1998). *Monthly Weather Review*, *136*(6), 2047–2065. https://doi.org/10.1175/2007MWR2051.1

Evans, C., Wood, K. M., Aberson, S. D., Archambault, H. M., Milrad, S. M., Bosart, L. F., et al. (2017). The extratropical transition of tropical cyclones. Part I: Cyclone evolution and direct impacts. *Monthly Weather Review*, *145*(11), 4317–4344. https://doi.org/10.1175/MWR-D-17-0027.1

Feldmann, M., Emanuel, K., Zhu, L., & Lohmann, U. (2019). Estimation of Atlantic tropical cyclone rainfall frequency in the United States. *Journal of Applied Meteorology and Climatology*, *58*(8), 1853–1866. https://doi.org/10.1175/JAMC-D-19-0011.1

Fritz, H. M., Blount, C., Sokoloski, R., Singleton, J., Fuggle, A., McAdoo, B. G., et al. (2007). Hurricane Katrina storm surge distribution and field observations on the Mississippi Barrier Islands. *Estuarine, Coastal and Shelf Science*, *74*(1–2), 12–20. https://doi.org/10.1016/j.ecss.2007.03.015

Galarneau, T. J., Davis, C. A., & Shapiro, M. A. (2013). Intensification of Hurricane Sandy (2012) through extratropical warm core seclusion. *Monthly Weather Review*, *141*(12), 4296–4321. https://doi.org/10.1175/MWR-D-13-00181.1

Gori, A., & Lin, N. (2022). North Atlantic TC size and storm tide reconstructions, 1950-2020 [Dataset]. *DesignSafe-CI*. https://doi.org/10.17603/ds2-t051-ew98v1

Gori, A., Lin, N., Xi, D., & Emanuel, K. (2022). Tropical cyclone climatology change greatly exacerbates US extreme rainfall–surge hazard. *Nature Climate Change*, *12*(2), 171–178. https://doi.org/10.1038/s41558-021-01272-7

Haigh, I. D., MacPherson, L. R., Mason, M. S., Wijeratne, E. M. S., Pattiaratchi, C. B., Crompton, R. P., & George, S. (2014). Estimating present day extreme water level exceedance probabilities around the coastline of Australia: Tropical cyclone-induced storm surges. *Climate Dynamics*, *42*(1–2), 139–157. https://doi.org/10.1007/s00382-012-1653-0

Halverson, J. B., & Rabenhorst, T. (2013). Hurricane Sandy: The science and impacts of a superstorm. *Weatherwise*, *66*(2), 14–23. https://doi.org/10.1080/00431672.2013.762838

Hart, R. E. (2001). *The extratropical transition of Atlantic tropical cyclones: Climatology, lifecycle definition, and a case study*. Pennsylvania State University.

Hart, R. E. (2003). A cyclone phase space derived from thermal wind and thermal asymmetry. *Monthly Weather Review*, *131*(4), 585–616. https://doi.org/10.1175/1520-0493(2003)131<0585:ACPSDF>2.0.CO;2

Hart, R. E., & Evans, J. L. (2001). A climatology of the extratropical transition of Atlantic tropical cyclones. *Journal of Climate*, *14*(4), 546–564. https://doi.org/10.1175/1520-0442(2001)014<0546:ACOTET>2.0.CO;2

Hatzikyriakou, A., Lin, N., Gong, J., Xian, S., Hu, X., & Kennedy, A. (2016). Component-based vulnerability analysis for residential structures subjected to storm surge impact from hurricane Sandy. *Natural Hazards Review*, *17*(1), 05015005. https://doi.org/10.1061/(asce)nh.1527-6996.0000205

Hersbach, H., Bell, B., Berrisford, P., Hirahara, S., Horányi, A., Muñoz-Sabater, J., et al. (2020). The ERA5 global reanalysis. *Quarterly Journal of the Royal Meteorological Society*, *146*(730), 1999–2049. https://doi.org/10.1002/qj.3803

Hlywiak, J., & Nolan, D. S. (2021). The response of the near-surface tropical cyclone wind field to inland surface roughness length and soil moisture content during and after landfall. *Journal of the Atmospheric Sciences*, *78*(3), 983–1000. https://doi.org/10.1175/JAS-D-20-0211.1

Hodges, K., Cobb, A., & Vidale, P. L. (2017). How well are tropical cyclones represented in reanalysis datasets? *Journal of Climate*, *30*(14), 5243–5264. https://doi.org/10.1175/JCLI-D-16-0557.1

Holland, G. (1980). An analytical model of wind and pressure profiles in hurricanes. *Monthly Weather Review*, *108*(8), 1212–1218. https://doi.org/10.1175/1520-0493(1980)108<1212:aamotw>2.0.co;2

Huffman, G. J., & Pendergrass, A., & NCAR. (2021). The climate data guide: TRMM: Tropical rainfall measuring mission. [WWW Document].

Irish, J. L., Resio, D. T., & Ratcliff, J. J. (2008). The influence of storm size on hurricane surge. *Journal of Physical Oceanography*, *38*(9), 2003–2013. https://doi.org/10.1175/2008JPO3727.1

Jones, S. C., Harr, P. A., Abraham, J., Bosart, L. F., Bowyer, P. J., Evans, J. L., et al. (2003). The extratropical transition of tropical cyclones: Forecast challenges, current understanding, and future directions. *Weather and Forecasting*, *18*(6), 1052–1092. https://doi.org/10.1175/1520-0434(2003)018<1052:TETOTC>2.0.CO;2

Klotz, B. W., & Nolan, D. S. (2019). SFMR surface wind undersampling over the tropical cyclone life cycle. *Monthly Weather Review*, *147*(1), 247–268. https://doi.org/10.1175/MWR-D-18-0296.1

Knabb, R. D., Rhome, J. R., & Brown, D. P. (2005). Tropical cyclone report: Hurricane Katrina.
Knaff, J. A., Sampson, C. R., & Musgrave, K. D. (2018). Statistical tropical cyclone wind radii prediction using climatology and persistence: Updates for the western North Pacific. *Weather and Forecasting*, *33*(4), 1093–1098. https://doi.org/10.1175/WAF-D-18-0027.1
Knaff, J. A., & Zehr, R. M. (2007). Reexamination of tropical cyclone wind-pressure relationships. *Weather and Forecasting*, *22*(1), 71–88. https://doi.org/10.1175/WAF965.1
Knapp, K. R., Kruk, M. C., Levinson, D. H., Diamond, H. J., & Neumann, C. J. (2010). The international best track archive for climate stewardship (IBTrACS). *Bulletin of the American Meteorological Society*, *91*(3), 363–376. https://doi.org/10.1175/2009BAMS2755.1
Kossin, J. P., Olander, T. L., & Knapp, K. R. (2013). Trend analysis with a new global record of tropical cyclone intensity. *Journal of Climate*, *26*(24), 9960–9976. https://doi.org/10.1175/JCLI-D-13-00262.1
Landsea, C. W., Anderson, C., Charles, N., Clark, G., Dunion, J., Fernandez-Partagas, J., et al. (2004). The Atlantic hurricane database re-analysis project: Documentation for the 1851-1910 alterations and additions to the HURDAT database. *Hurricanes and Typhoons: Past, Present, and Future*, *177*, 221.
Landsea, C. W., & Franklin, J. L. (2013). Atlantic hurricane database uncertainty and presentation of a new database format. *Monthly Weather Review*, *141*(10), 3576–3592. https://doi.org/10.1175/MWR-D-12-00254.1
Lin, N., & Chavas, D. (2012). On hurricane parametric wind and applications in storm surge modeling. *Journal of Geophysical Research*, *117*(D9), 1–19. https://doi.org/10.1029/2011JD017126
Lin, N., Emanuel, K., Oppenheimer, M., & Vanmarcke, E. (2012). Physically based assessment of hurricane surge threat under climate change. *Nature Climate Change*, *2*(6), 462–467. https://doi.org/10.1038/nclimate1389
Lin, N., Emanuel, K. A., Smith, J. A., & Vanmarcke, E. (2010). Risk assessment of hurricane storm surge for New York City. *Journal of Geophysical Research*, *115*(D18), 1–11. https://doi.org/10.1029/2009JD013630
Lin, N., Lane, P., Emanuel, K. A., Sullivan, R. M., & Donnelly, J. P. (2014). Heightened hurricane surge risk in northwest Florida revealed from climatological-hydrodynamic modeling and paleorecord reconstruction. *Journal of Geophysical Research: Atmospheres*, *119*(14), 8606–8623. https://doi.org/10.1002/2014JD021584
Lin, N., Smith, J. A., Villarini, G., Marchok, T. P., & Baeck, M. L. (2010). Modeling extreme rainfall, winds, and surge from hurricane Isabel (2003). *Weather and Forecasting*, *25*(5), 1342–1361. https://doi.org/10.1175/2010waf2222349.1
Lin, Y., & Mitchell, K. E. (2005). The NCEP stage II/IV hourly precipitation analyses: Development and applications. In *Proceedings of the 19th conference hydrology, American meteorological society*.
Liu, M., Vecchi, G. A., Smith, J. A., & Knutson, T. R. (2019). Causes of large projected increases in hurricane precipitation rates with global warming. *NPJ Climate and Atmospheric Science*, *2*, 1–5. https://doi.org/10.1038/s41612-019-0095-3
Luettich, R. A., Westerink, J. J., & Scheffner, N. W. (1992). ADCIRC: An advanced three-dimensional circulation model for shelves, coasts, and estuaries. Report 1: Theory and methodology of ADCIRC-2DDI and ADCIRC-3DL.
Marsooli, R., & Lin, N. (2018). Numerical modeling of historical storm tides and waves and their interactions along the U.S. East and Gulf Coasts. *Journal of Geophysical Research: Oceans*, *123*(5), 3844–3874. https://doi.org/10.1029/2017JC013434
Marsooli, R., Lin, N., Emanuel, K., & Feng, K. (2019). Climate change exacerbates hurricane flood hazards along US Atlantic and Gulf Coasts in spatially varying patterns. *Nature Communications*, *10*, 1–9. https://doi.org/10.1038/s41467-019-11755-z
Menne, M. J., Durre, I., Vose, R. S., Gleason, B. E., & Houston, T. G. (2012). An overview of the global historical climatology network-daily database. *Journal of Atmospheric and Oceanic Technology*, *29*(7), 897–910. https://doi.org/10.1175/JTECH-D-11-00103.1
Merrill, R. (1984). A comparison of large and small tropical cyclones. *Monthly Weather Review*, *112*(7), 1408–1418. https://doi.org/10.1175/1520-0493(1984)112<1408:acolas>2.0.co;2
Moftakhari, H. R., Salvadori, G., AghaKouchak, A., Sanders, B. F., & Matthew, R. A. (2017). Compounding effects of sea level rise and fluvial flooding. *Proceedings of the National Academy of Sciences of the United States of America*, *114*(37), 9785–9790. https://doi.org/10.1073/pnas.1620325114
Muis, S., Lin, N., Verlaan, M., Winsemius, H. C., Ward, P. J., & Aerts, J. C. J. H. (2019). Spatiotemporal patterns of extreme sea levels along the western North-Atlantic coasts. *Scientific Reports*, *9*, 1–12. https://doi.org/10.1038/s41598-019-40157-w
Nasr, A. A., Wahl, T., Rashid, M. M., Camus, P., & Haigh, I. D. (2021). Assessing the dependence structure between oceanographic, fluvial, and pluvial flooding drivers along the United States coastline. *Hydrology and Earth System Sciences*, *25*(12), 6203–6222. https://doi.org/10.5194/hess-25-6203-2021
NBS. (1971). NBS technical note 569: Hurricane Camille—August 1969.
Needham, H. F., & Keim, B. D. (2012). A storm surge database for the US Gulf Coast. *International Journal of Climatology*, *32*(14), 2108–2123. https://doi.org/10.1002/joc.2425
Needham, H. F., Keim, B. D., & Sathiaraj, D. (2015). A review of tropical cyclone-generated storm surges: Global data sources, observations, and impacts. *Reviews of Geophysics*, *53*(2), 545–591. https://doi.org/10.1002/2014RG000477
Nguyen, L. T., Molinari, J., & Thomas, D. (2014). Evaluation of tropical cyclone center identification methods in numerical models. *Monthly Weather Review*, *142*(11), 4326–4339. https://doi.org/10.1175/MWR-D-14-00044.1
Nofal, O. M., van de Lindt, J. W., Do, T. Q., Yan, G., Hamideh, S., Cox, D. T., & Dietrich, J. C. (2021). Methodology for regional multihazard hurricane damage and risk assessment. *Journal of Structural Engineering*, *147*(11), 04021185. https://doi.org/10.1061/(asce)st.1943-541x.0003144
Pilkington, S. F., & Mahmoud, H. N. (2016). Using artificial neural networks to forecast economic impact of multi-hazard hurricane-based events. *Sustainable and Resilient Infrastructure*, *1*(1–2), 63–83. https://doi.org/10.1080/23789689.2016.1179529
Powell, M. D., Houston, S. H., Amat, L. R., & Morisseau-Leroy, N. (1998). The HRD real-time hurricane wind analysis system. *Journal of Wind Engineering and Industrial Aerodynamics*, *77*(78), 53–64. https://doi.org/10.1016/S0167-6105(98)00131-7
Pugh, D. (1987). *Tides, surges and mean seasea-level*. John Wiley & Sons.
Ramos-Valle, A. N., Curchitser, E. N., & Bruyère, C. L. (2020). Impact of tropical cyclone landfall angle on storm surge along the Mid-Atlantic bight. *Journal of Geophysical Research: Atmospheres*, *125*(4), 1–19. https://doi.org/10.1029/2019JD031796
Sarro, G., & Evans, C. (2022). An updated investigation of post-transformation intensity, structural, and duration extremes for extratropically transitioning North Atlantic tropical cyclones. *Monthly Weather Review*, *150*(11), 2911–2933. https://doi.org/10.1175/MWR-D-22-0088.1
Schenkel, B. A., & Hart, R. E. (2012). An examination of tropical cyclone position, intensity, and intensity life cycle within atmospheric reanalysis datasets. *Journal of Climate*, *25*(10), 3453–3475. https://doi.org/10.1175/2011JCLI4208.1
Schenkel, B. A., Lin, N., Chavas, D., Oppenheimer, M., & Brammer, A. (2017). Evaluating outer tropical cyclone size in reanalysis datasets using QuikSCAT data. *Journal of Climate*, *30*(21), 8745–8762. https://doi.org/10.1175/JCLI-D-17-0122.1
Schenkel, B. A., Lin, N., Chavas, D., Vecchi, G. A., Oppenheimer, M., & Brammer, A. (2018). Lifetime evolution of outer tropical cyclone size and structure as diagnosed from reanalysis and climate model data. *Journal of Climate*, *31*(19), 7985–8004. https://doi.org/10.1175/JCLI-D-17-0630.1

Smith, A. B., & Katz, R. W. (2013). US billion-dollar weather and climate disasters: Data sources, trends, accuracy and biases. *Natural Hazards*, *67*(2), 387–410. https://doi.org/10.1007/s11069-013-0566-5

Song, J. Y., Alipour, A., Moftakhari, H. R., & Moradkhani, H. (2020). Toward a more effective hurricane hazard communication. *Environmental Research Letters*, *15*(6), 064012. https://doi.org/10.1088/1748-9326/ab875f

Stiles, B. W., Danielson, R. E., Poulsen, W. L., Brennan, M. J., Hristova-Veleva, S., Shen, T. P., & Fore, A. G. (2014). Optimized tropical cyclone winds from QuikSCAT: A neural network approach. *IEEE Transactions on Geoscience and Remote Sensing*, *52*(11), 7418–7434. https://doi.org/10.1109/TGRS.2014.2312333

Taylor, K. E. (2001). Summarizing multiple aspects of model performance in a single diagram. *Journal of Geophysical Research*, *106*(D7), 7183–7192. https://doi.org/10.1029/2000jd900719

Thomas, A., Dietrich, J. C., Asher, T. G., Bell, M., Blanton, B. O., Copeland, J. H., et al. (2019). Influence of storm timing and forward speed on tides and storm surge during Hurricane Matthew. *Ocean Modelling*, *137*, 1–19. https://doi.org/10.1016/j.ocemod.2019.03.004

Thorne, P. W., & Vose, R. S. (2010). Reanalyses suitable for characterizing long-term trends. *Bulletin of the American Meteorological Society*, *91*(3), 353–361. https://doi.org/10.1175/2009BAMS2858.1

Uhlhorn, E. W., & Nolan, D. S. (2012). Observational undersampling in tropical cyclones and implications for estimated intensity. *Monthly Weather Review*, *140*(3), 825–840. https://doi.org/10.1175/MWR-D-11-00073.1

Wahl, T., Jain, S., Bender, J., Meyers, S. D., & Luther, M. E. (2015). Increasing risk of compound flooding from storm surge and rainfall for major US cities. *Nature Climate Change*, *5*(12), 1–6. https://doi.org/10.1038/NCLIMATE2736

Wang, S., Lin, N., & Gori, A. (2022a). Investigation of tropical cyclone wind models with application to storm tide simulations. *Journal of Geophysical Research: Atmospheres*, *127*(17), e2021JD036359. https://doi.org/10.1029/2021JD036359

Wang, S., Lin, N., & Gori, A. (2022b) New wind forcing option (CLE15 wind model) for hurricane surge simulation with ADCIRC. [Software]. *DesignSafe-CI*. https://doi.org/10.17603/ds2-xd0r-bk81v1

Westerink, J. J., Luettich, R. A., Blain, C. A., & Scheffner, N. W. (1992). ADCIRC: An advanced three-dimensional circulation model for shelves, coasts, and estuaries. Report 2: User's Manual for ADCIRC-2DDI.

Willmott, C. J. (1981). On the validation of models. *Physical Geography*, *2*, 184–194. https://doi.org/10.1080/02723646.1981.10642213

Willoughby, H. E., Darling, R. W. R., & Rahn, M. E. (2006). Parametric representation of the primary hurricane vortex. Part II: A new family of sectionally continuous profiles. *Monthly Weather Review*, *134*(4), 1102–1120. https://doi.org/10.1175/MWR3106.1

Woodruff, J. D., Irish, J. L., & Camargo, S. J. (2013). Coastal flooding by tropical cyclones and sea-level rise. *Nature*, *504*(7478), 44–52. https://doi.org/10.1038/nature12855

Xi, D., Lin, N., & Smith, J. (2020). Evaluation of a physics-based tropical cyclone rainfall model for risk assessment. *Journal of Hydrometeorology*, *21*(9), 2197–2218. https://doi.org/10.1175/JHM-D-20-0035.1

Zhang, W., Villarini, G., Vecchi, G. A., & Smith, J. A. (2018). Urbanization exacerbated the rainfall and flooding caused by hurricane Harvey in Houston. *Nature*, *563*(7731), 384–388. https://doi.org/10.1038/s41586-018-0676-z

Zhu, L., Quiring, S. M., & Emanuel, K. A. (2013). Estimating tropical cyclone precipitation risk in Texas. *Geophysical Research Letters*, *40*(23), 6225–6230. https://doi.org/10.1002/2013GL058284